Identifying droplet boundaries: Impacts of surface topography on droplet freezing and an investigation of the impacts of surfactant on sprayed droplet dynamics

by

Emily M. Stallbaumer-Cyr

B.S., Kansas State University, 2018

AN ABSTRACT OF A DISSERTATION

submitted in partial fulfillment of the requirements for the degree

DOCTOR OF PHILOSOPHY

Alan Levin Department of Mechanical and Nuclear Engineering
Carl R. Ice College of Engineering

KANSAS STATE UNIVERSITY
Manhattan, Kansas

2023

Abstract

The formation and behavior of droplets is critical in many applications, including freezing [1-8], irrigation [9-11], heat transfer [12-14], spread of disease via respiratory droplets [15, 16], and precipitation [6, 17]. There are two research foci of this dissertation: 1) condensing droplets subsequently freezing on surfaces, and 2) droplet spray dynamics from irrigation nozzles. Freezing of droplets can cause a wide variety of problems, including frosting on windshields; icing on wind turbines and airplanes; and freezing of heat pipes, thereby reducing their ability for thermal management. Droplets also form from spray break up (e.g., irrigation and pesticides), which are critical for agricultural applications and water conservation. Water scarcity (i.e., water demand is greater than water supply and water resources [18]) is increasingly becoming an issue globally; in 2016, 71% of the global population experienced water scarcity for at least 1 month/year.

This research investigates the freezing mechanisms of droplets on grooved and sintered wick surfaces found in commercial heat pipes compared to a plain copper surface. The freezing times were quantified and the different propagation mechanism (ice bridging, frost halos, and cascade freezing) were explored. The surfaces were observed for one hour under a microscope, with controlled conditions (i.e., the ambient temperature was 22°C, the relative humidity was 60%, and the surface temperature was set to -5°C). Freezing occurred earliest on the plain copper surface at 6.3 minutes and took the shortest amount of time to completely freeze (i.e., 4.6 minutes); the freezing front propagated via ice bridging with little to no interruptions. The grooved surface began freezing at 12.5 minutes and took 8.3 minutes to completely freeze. The freezing front on the grooved wick propagated via ice bridging, but took longer to freeze due to each individual groove propagating independently. The sintered surface took the longest to freeze, beginning at 16.4 minutes and took 10.9 minutes to completely freeze. The sintered wick experienced propagation via ice bridging, stochastic freezing and cascade freezing; however, freezing propagation across the surface was delayed due to voids existing between the sintered particles that did not allow ice to propagate across the voids.

The addition of surfactant and its effects on spray dynamics and droplet formation was investigated using fan, full cone, and bubbler nozzles with the addition of a surfactant, Surfactin, at 0.1% concentration by weight added to distilled water, decreasing the surface tension from 72.8 mN/m to 29.2 mN/m. The fan nozzles were tested and observed at 30, 45, and 60 psi (206.8, 310.3,

and 413.7 kPa) and the full cone nozzle was observed at 20, 30, 45, and 60 psi (137.9, 206.8, 310.3, and 413.7 kPa). Both fan and full cone nozzles experienced second wind induced breakup of the liquid sheets exiting the nozzle; the addition of surfactant resulted in an increased breakup length and a decreased droplet size. The fan nozzle's volumetric median droplet diameter, D_{V50}, decreased with the addition of surfactant (e.g., the F1 nozzle decreased by 65.6 µm, 53 µm, and 26.3 µm at 30, 45, and 60 psi respectively). The full cone nozzle DV50 decreased initially with the addition of surfactant (27.8 µm, 14.3 µm, and 13.4 µm at 20, 30, and 45 psi, respectively), but increased the D_{V50} at 60 psi (24.3 µm). Sprays from 6, 10, and 15 psi bubbler nozzles were measured and observed to experience Rayleigh and first wind induced breakup. The addition of surfactant increased the diameter of the jet or ligament formed from the bubbler plate, thereby increasing the breakup length and the droplet size at 10 and 15 psi (droplet size decreased by 750.6 µm and 4462.7 µm, respectively). The effect of the surfactant on was not as significant for the 6 psi bubbler nozzle. The changes in droplet sizes have implications for drift (i.e., smaller droplets are more prone to drift), coverage, and infiltration of the sprayed fluid into the soil.

Identifying droplet boundaries: impacts of surface topography on droplet freezing and investigation of Surfactin on spraying dynamics

by

Emily M. Stallbaumer-Cyr

B.S., Kansas State University, 2018

A DISSERTATION

submitted in partial fulfillment of the requirements for the degree

DOCTOR OF PHILOSOPHY

Alan Levin Department of Mechanical and Nuclear Engineering
Carl. R. Ice College of Engineering

KANSAS STATE UNIVERSITY
Manhattan, Kansas

2023

Approved by:

Co-Major Professor
Dr. Amy R. Betz

Approved by:

Co-Major Professor
Dr. Melanie M. Derby

Copyright

Abstract

The formation and behavior of droplets is critical in many applications, including freezing [1-8], irrigation [9-11], heat transfer [9-11], spread of disease via respiratory droplets [12, 13], and precipitation [6, 14]. There are two research foci of this dissertation: 1) condensing droplets subsequently freezing on surfaces, and 2) droplet spray dynamics from irrigation nozzles. Freezing of droplets can cause a wide variety of problems, including frosting on windshields; icing on wind turbines and airplanes; and freezing of heat pipes, thereby reducing their ability for thermal management. Droplets also form from spray break up (e.g., irrigation and pesticides), which are critical for agricultural applications and water conservation. Water scarcity (i.e., water demand is greater than water supply and water resources [15]) is increasingly becoming an issue globally; in 2016, 71% of the global population experienced water scarcity for at least 1 month/year.

This research investigates the freezing mechanisms of droplets on grooved and sintered wick surfaces found in commercial heat pipes compared to a plain copper surface. The freezing times were quantified and the different propagation mechanism (ice bridging, frost halos, and cascade freezing) were explored. The surfaces were observed for one hour under a microscope, with controlled conditions (i.e., the ambient temperature was 22°C, the relative humidity was 60%, and the surface temperature was set to -5°C). Freezing occurred earliest on the plain copper surface at 6.3 minutes and took the shortest amount of time to completely freeze (i.e., 4.6 minutes); the freezing front propagated via ice bridging with little to no interruptions. The grooved surface began freezing at 12.5 minutes and took 8.3 minutes to completely freeze. The freezing front on the grooved wick propagated via ice bridging, but took longer to freeze due to each individual groove propagating independently. The sintered surface took the longest to freeze, beginning at 16.4 minutes and took 10.9 minutes to completely freeze. The sintered wick experienced propagation via ice bridging, stochastic freezing and cascade freezing; however, freezing propagation across the surface was delayed due to voids existing between the sintered particles that did not allow ice to propagate across the voids.

The addition of surfactant and its effects on spray dynamics and droplet formation was investigated using fan, full cone, and bubbler nozzles with the addition of a surfactant, Surfactin, at 0.1% concentration by weight added to distilled water, decreasing the surface tension from 72.8 mN/m to 29.2 mN/m. The fan nozzles were tested and observed at 30, 45, and 60 psi (206.8, 310.3,

and 413.7 kPa) and the full cone nozzle was observed at 20, 30, 45, and 60 psi (137.9, 206.8, 310.3, and 413.7 kPa). Both fan and full cone nozzles experienced second wind induced breakup of the liquid sheets exiting the nozzle; the addition of surfactant resulted in an increased breakup length and a decreased droplet size. The fan nozzle's volumetric median droplet diameter, DV50, decreased with the addition of surfactant (e.g., the F1 nozzle decreased by 65.6 μm, 53 μm, and 26.3 μm at 30, 45, and 60 psi respectively). The full cone nozzle DV50 decreased initially with the addition of surfactant (27.8 μm, 14.3 μm, and 13.4 μm at 20, 30, and 45 psi, respectively), but increased the DV50 at 60 psi (24.3 μm). Sprays from 6, 10, and 15 psi bubbler nozzles were measured and observed to experience Rayleigh and first wind induced breakup. The addition of surfactant increased the diameter of the jet or ligament formed from the bubbler plate, thereby increasing the breakup length and the droplet size at 10 and 15 psi (droplet size decreased by 750.6 μm and 4462.7 μm, respectively). The effect of the surfactant on was not as significant for the 6 psi bubbler nozzle. The changes in droplet sizes have implications for drift (i.e., smaller droplets are more prone to drift), coverage, and infiltration of the sprayed fluid into the soil.

Table of Contents

List of Figures

List of Tables

Acknowledgments

I would like to thank Dr. Melanie Derby and Dr. Amy Betz for being my major professors and for all of their insight, advice, and encouragement. They have both taught me so much through the years and continuously inspire me. Additionally, I would like to thank Dr. Betz for inspiring and encouraging me to attend graduate school. I would also like to thank Dr. Mingjun Wei and Dr. Bret Flanders for being members of my committee and sharing ideas and feedback. I would like to thank Dr. Jonathan Aguilar for his assistance with the bubbler nozzles and understanding irrigation.

I would like to thank IER for allowing me use of their environmental chamber. I would like to thank NSF for funding with Grants #1651451 and #1828571. I would also like to thank the members of the CHILLAB and M&M Lab for their support, help, and walking breaks through the years.

Finally, I would like to thank my friends and family who have loudly cheered me on from the sidelines: Michael, Kat, Abigail, Antonio, Casey, Madeline, Amelia, Gennifer, Bailey, Dylan, Jordan, Katie, Molly, Faye, Todd, my church group, and so many others. A special thank you to my parents who told me I should be an engineer in middle school and I adamantly replied “no thanks.” Mom you were right – there it’s immortalized in my dissertation forever.

Dedication

I would like to dedicate my dissertation to my husband Damian Cyr; otherwise he survived my dissertation and all I got him was a sticker. In all seriousness, Damian, thank you for your unwavering support and encouragement, sticking with me through the highs and lows, and learning more about droplets than you likely ever anticipated. It means more to me than words could ever say.

Preface

Chapter 2 - , parts of Chapter 1 - , and parts of Chapter 6 - are reproduced from [1] E. M. Stallbaumer-Cyr, M. M. Derby, and A. R. Betz, "Physical mechanisms for delaying condensation freezing on grooved and sintered wicking surfaces," Applied Physics Letters, vol. 121, p. 071601, 2022., with permission from AIP publishing.

Chapter 1 - Introduction

The formation and behavior of droplets is critical in many applications, including freezing [1-8], irrigation [9-11], heat transfer [12-14], spread of disease via respiratory droplets [15, 16], and precipitation [6, 17]. The focus of this dissertation is 1) condensing droplets subsequently freezing on surfaces and 2) droplet spray dynamics from irrigation nozzles. The mechanisms of droplets condensing on surfaces is impacted by surface properties such as surface geometry, surface tension, and roughness. The surface affects the nucleation, location, and size of droplets. Condensation droplet formation has connotations in cooling, windshield fogging, etc. Further, if the droplets are exposed to freezing temperatures, the surface impacts the initial freezing and freezing propagation of the surface. Frozen droplets cause problems in everyday things such as windshield frost and icing on wind turbines and airplanes [2, 8, 19, 20]. For the years of 2002-2005, airports in the United States used 25.042 million gallons/year of aircraft deicing and anti-icing fluid [20]. Less visible, freezing in heat pipes can be incredibly damaging.

Heat pipes are a critical component in heat management systems, from laptops [21] to spacecraft [22]; the usefulness of heat pipes comes from their ability to passively transfer heat without additional equipment [21, 23-26]. For space applications, heat pipes can be exposed to the freezing temperatures of space – resulting in the solidification of the working fluid [26, 27], thereby reducing or preventing function [26, 28], decreasing performance [29], or damaging the wick [27, 29]. Current heat pipe freezing research focuses primarily on start-up from a frozen state [24, 26, 27, 30, 31] and liquid control methods to prevent ice plugs (i.e. gas-charged heat pipes) [24, 26, 28, 31].[1]

Limited data exist on the freezing process in the heat pipes. Current research on freezing via condensation (i.e., condensation frosting) focuses primarily on flat surfaces [32-34] or surfaces designed to delay freezing or promote easy ice removal, such as coatings and hydrophobic surfaces [2, 3, 35-37], micropillars, microgrooves [5, 38-40], chemical etching, and nanopillars [4, 5, 40-42]. Surface characteristics, such as hydrophobicity [2, 40], surface topography [39, 40, 42-44],

[1] Reproduced from E. M. Stallbaumer-Cyr, M. M. Derby, and A. R. Betz, "Physical mechanisms for delaying condensation freezing on grooved and sintered wicking surfaces," Applied Physics Letters, vol. 121, p. 071601, 2022., with permission from AIP publishing

surface roughness [5, 45], and surface tension [5, 45] affect behaviors such as droplet nucleation, droplet sizes, time freezing begins, and freezing propagation.[1]

Droplets also form from spray break up (e.g., irrigation and pesticides). Spray dynamics are of particular interest in agriculture; if pesticide droplets are too big, they will not be as effective in their purpose, but if they are too small, they risk drifting to other crops or water sources. In irrigation, optimizing water droplets is imperative to reducing water use. Water scarcity (i.e., water demand is greater than water supply and water resources [18]) is increasingly becoming an issue globally; in 2016, 71% of the global population experienced water scarcity for at least 1 month/year [46]. In the last two decades, the available freshwater per person globally decreased by 20% [47]. While available water continues to decrease, population is expected to continue to increase; the world population is anticipated to reach 9.7 billion by 2050 [48]. Water is necessary for a myriad of different reasons in everyday life, culminating in the Food-Energy-Water Nexus: water, food production, and power production. Water is connected to food production via irrigation and livestock; to power production via power source, cooling source, and pumping water; power is connected to food via planting, harvesting, directing water, and food processing. Agriculture is the largest use of water both globally (70% of freshwater use) and within the United States (42% of freshwater use) [9, 18, 47, 49-53]. In Kansas, a primarily agricultural-based state, irrigation accounts for 83% of water use [51]. The impact of irrigation is reflected in the land prices, in 2022 the value of land in Kansas for non-irrigated cropland was $2,950 while the value for irrigated cropland was $4,000 [54]. While, globally, irrigated cropland is 20% of all cropland, it produces 40% of the global crop production [9, 47].

Chapter 2 - Condensation Droplet Formation and Freezing[2]

2.1 Physical mechanisms for delaying condensation freezing on grooved and sintered wicking surfaces

The research objectives of this work are to investigate and compare condensation freezing on commercial heat pipe wicks (i.e., grooved and sintered wicks) and a plain copper surface. This research will illuminate freezing mechanisms, quantify freezing times, and explain freezing propagation on complex three-dimensional surfaces. This fundamental understanding of freezing mechanisms in three dimensions is vital to the future design of heat pipes where performance is not prevented or impeded by freezing.

The Gibbs free energy barrier must be overcome for initial condensation nucleation and freezing to begin on the surface; the Gibbs free energy barrier is impacted by the surface tension and the droplet diameter (i.e., larger droplets take more energy to freeze)[3, 4, 32, 55-57]. The change in Gibbs free energy equation is [32, 55]:

$$\Delta G = V_I \Delta \tilde{g}_V + \sigma_{IL} A_{IL} + (\sigma_{Iw} - \sigma_{wL}) A_{Iw} \qquad \mathbf{1}$$

where V_I is the volume of the ice embryo, $\tilde{g}_V$ is the change in energy per volume between water and ice, A is the contact area, and σ is the surface tension; the subscripts V, I, L, and w stand for volumetric, ice, liquid water, and the wall of the surface, respectively. Changes in the droplet volume, contact angle, and contact area of the droplet will change the Gibbs free energy barrier, thereby changing when freezing occurs. Increasing the volume of the ice embryo will also increase the contact area between the ice and liquid phases and/or the contact area between the ice and the wall of the surface, resulting in an overall increase of the change in Gibbs free energy. Altering the surface's wettability to increase the surface tension between the droplet and the surface will also result in an increase of the change in Gibbs free energy. Additionally, increasing the surface tension will likely result in an increased area between the droplet and the surface, further increasing the change in Gibbs free energy. Increasing the change in Gibbs free energy will require more energy for droplets to change from liquid to ice. However, surface modifications to change the Gibbs free energy are limited for heat pipes due to the necessity of the wick to transport liquids.

---

[2] Reproduced from E. M. Stallbaumer-Cyr, M. M. Derby, and A. R. Betz, "Physical mechanisms for delaying condensation freezing on grooved and sintered wicking surfaces," Applied Physics Letters, vol. 121, p. 071601, 2022., with permission from AIP publishing

On surfaces, the initial freezing frequently occurs on either the edges or on defects/rougher locations on the surface, due to the lowered Gibbs free energy [5, 57, 58]. After the initial freezing, the freezing front propagates along the surfaces via frozen droplets' interactions with liquid droplets. Ice bridging is the main propagation mechanism for the majority of surfaces investigated; water from a liquid droplet evaporates due to the proximity of a frozen droplet and the difference in pressure between the liquid droplet and the frozen droplet [7, 8, 19, 32, 57]. The water vapor reaches the frozen droplet, causing vapor to condense and freeze, thereby creating a bridge between the two droplets. When the bridge reaches the neighboring liquid droplet, it freezes that droplet; however, if the bridging parameter, S^* is greater than one, the droplet will evaporate completely before the ice bridge reaches the liquid droplet, creating a dry zone [7, 8, 32, 59]. Dry zones are areas in which frozen droplets and the neighboring droplets cannot interact. The bridging parameter is defined as $S^* = L_{max}/d$ where L_{max} is the largest distance between the two droplets and d is the liquid droplet's diameter [7, 8, 59]. Frost halos occur when a droplet initially freezes; the vapor pressure of the ice is greater than the vapor pressure of the liquid, thereby expelling vapor from the freezing droplet and condensing on the surrounding surface where the new droplets freeze [8, 19, 32]. Similar to frost halos, cascade freezing occurs when vapor is expelled from the freezing droplet; however, the vapor, along with airborne dust, impinges on the neighboring droplets and induces freezing instead of impinging and condensing on the surface [19, 60].

For this research, a plain copper surface, two copper sintered wick surfaces (Adv Thermal Solutions, ATSHP-F8L150S45W-455, flat heat pipe, 9.45mm wide), and two copper grooved wick surfaces (Adv Thermal Solutions, ATS-HPD6L300G30W-00, round heat pipe, 6.0mm in diameter) were investigated. The sintered and grooved wick surfaces are from commercially available heat pipes; the heat pipes were cut in half lengthwise and split into 25-mm-long sections. The surfaces were placed on a Peltier cooler under a Confocal Microscope. The surface temperature was set to -5°C and the surfaces were observed for approximately 1-hour, sufficient time for the surfaces to completely freeze. The freezing start time is the first instance of observable solidification of condensed water droplets and the freezing end time corresponds to the time when the observed surface is completely covered in ice. The freezing times were determined by observing locations near the center of the surfaces. The length of freezing is taken as the freezing end time minus the freezing start time [61]. Further discussion on the Experimental Apparatus can be found in Section 2.2.

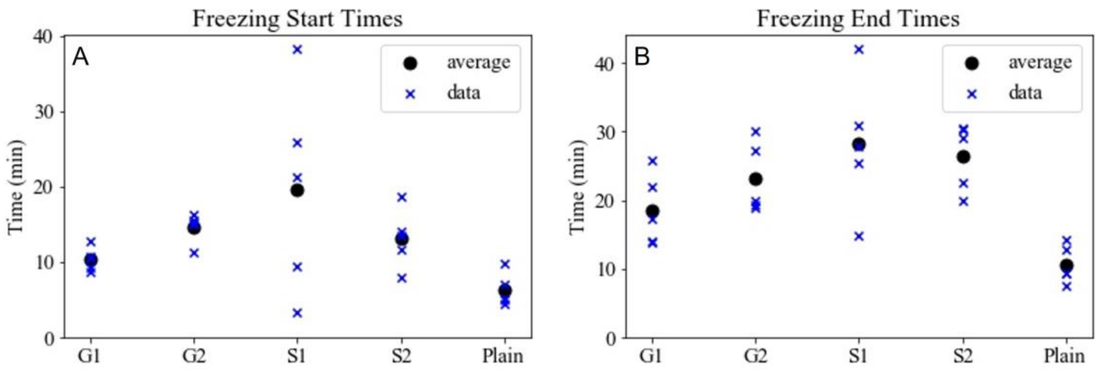

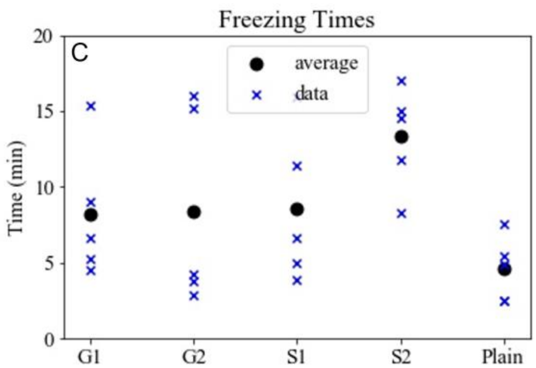

D	Average Start Time (min)		Average End Time (min)		Average Freezing Time (min)	
Plain		6.3		10.7		4.6
G1	10.4	12.5	18.6	20.8	8.2	8.3
G2	14.7		23.1		8.4	
S1	19.7	16.4	28.2	27.3	8.6	10.9
S2	13.2		26.5		13.3	

Figure 2.1 Graphs and table indicating the start, end, and freezing times of the surfaces. (A) The freezing start times of the individual replicates on the different surfaces. (B) The freezing end times of the individual replicates on the different surfaces. (C) The time it takes the surfaces to freeze from start to finish. (D) A table of the averages of the start time, end time, and freezing time.

Freezing was observed on five surfaces [i.e., Plain, Grooved 1 (G1), Grooved 2 (G2), Sintered 1 (S1), and Sintered 2 (S2)]; five replicates were conducted for each surface. The freezing times are shown in Figure 2.1. Additional experiments were performed on the Grooved 2, Sintered 2, and Plain copper surfaces at increased magnification to determine the size of droplets at freezing. Freezing is determined by the change in optical properties (transmittance and reflectance) of droplets. The histograms of droplet diameters at the time of freezing are shown in Figure 2.2. On the plain copper surface, freezing began after 6.3 minutes, on average. After freezing was initiated on the plain copper surface, the observed surface completely froze after an average of 4.6 minutes. The droplet diameters at freezing ranged widely on the plain copper surface, from 43.6 µm–418.5 µm, with an average diameter of 141.9 ± 58.1 µm (Figure 2.2A). Ice bridging is identified as the main freezing mechanism propelling the freezing front on the plain copper surface (Figure 2.3), consistent with previous literature regarding freezing fronts on smooth surfaces [2, 7, 8, 42]. Figure 2.3A depicts a frozen droplet on the plain surface that, as shown in Figure 2.3B, grows an ice bridge to its neighboring droplet, initiating freezing in the neighboring droplet, as depicted in

Figure 2.2D. The newly frozen droplet then also creates an ice bridge to initiate freezing in one of its neighboring droplets (Figure 2.3C).

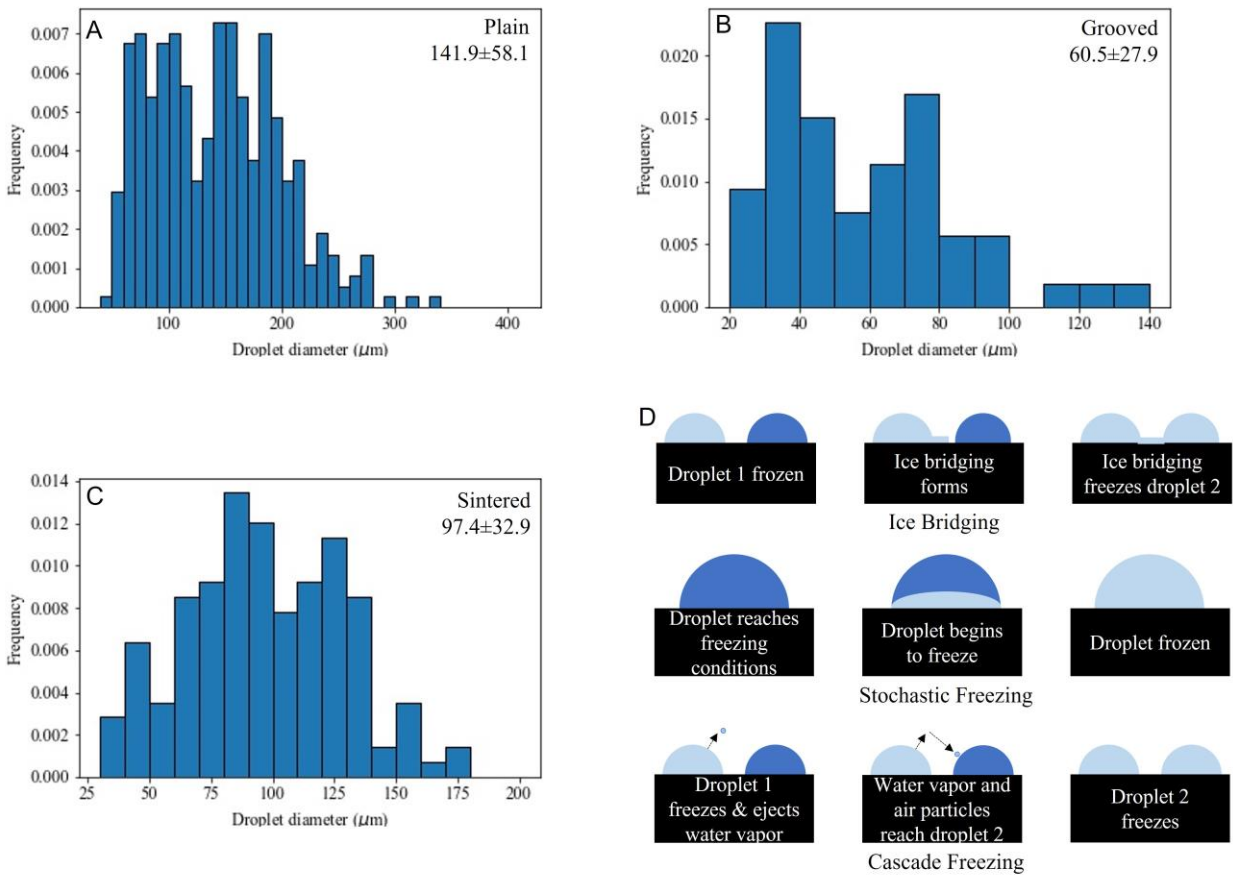

Figure 2.2 Histograms of the size of frozen droplets from 5 experiments on the (A) Plain copper surface with a frozen droplet diameter range from 43.6 µm–418.5 µm, (B) Grooved 2 with a frozen droplet diameter range from 24.9 µm–142.7 µm, and (C) Sintered 2 with a frozen droplet diameter range from 33.9–203.1 µm. (D) Schematic of three droplet freezing mechanisms, ice bridging, stochastic freezing, and cascade freezing.

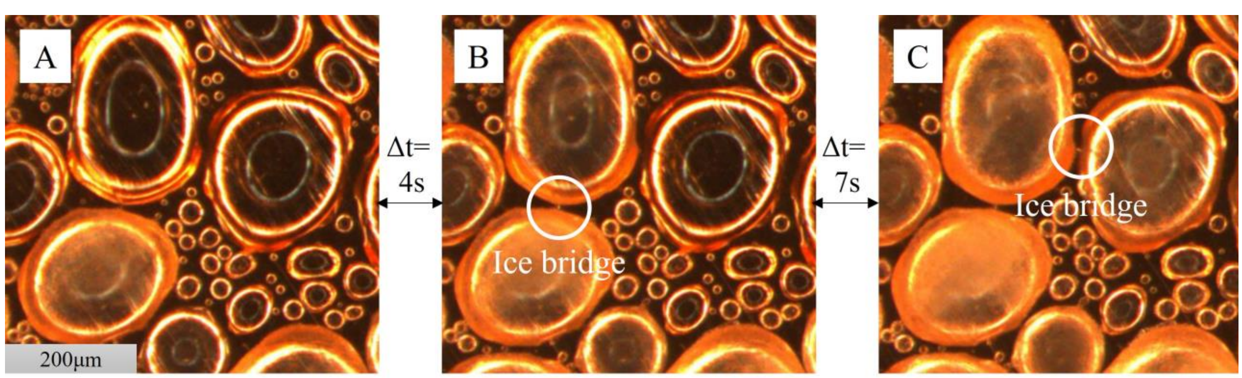

Figure 2.3 Droplets freezing on the plain surface (supplementary video). (A) a droplet freezing before bridging to its neighbor. (B) the frozen droplet bridging to its neighbor causing it to freeze. (C) the newly frozen droplet bridging to its neighbor causing it to freeze.

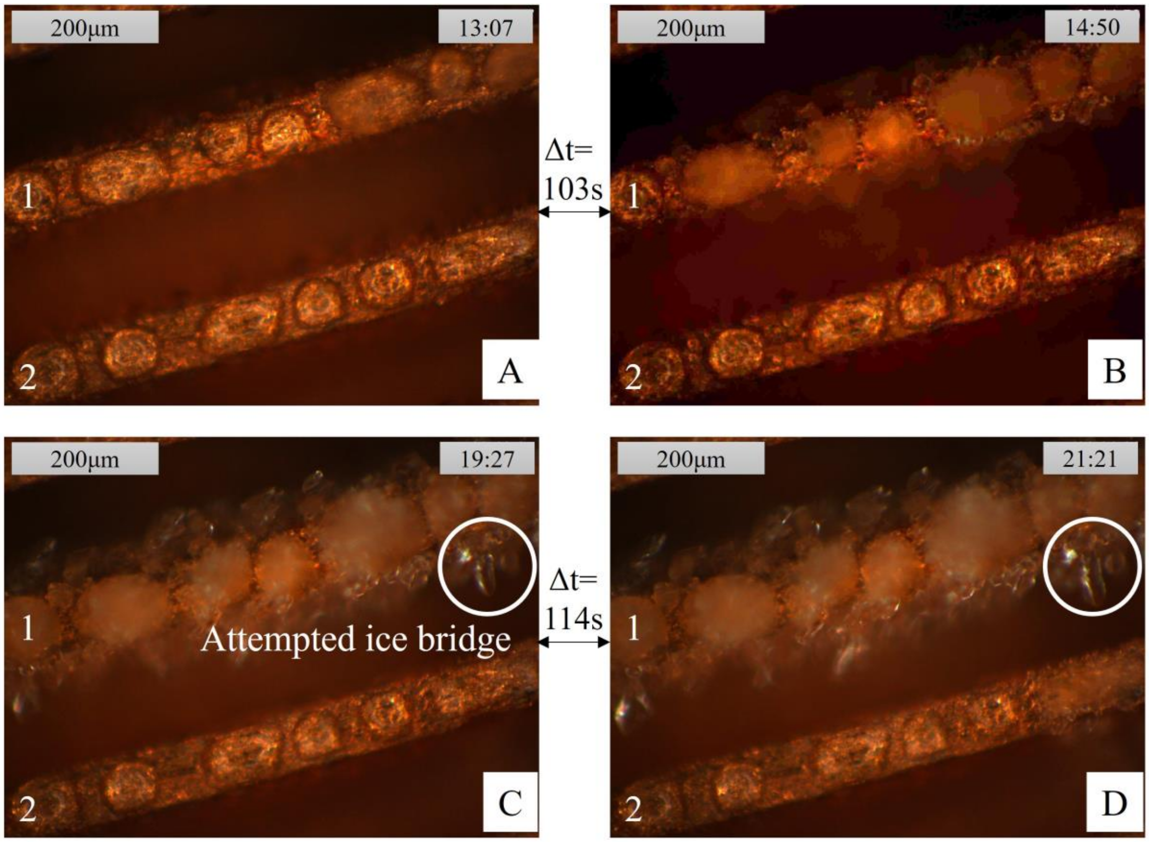

Figure 2.4 Droplets freezing on the top of two grooves in a grooved wick (i.e., the portion of the groove furthest from the Peltier cooler) (supplementary video). A) The droplets have begun to freeze on one of the grooves, B) the droplets on groove 1 are completely frozen, C) almost 4.5 minutes after the droplets on groove 1 froze, the droplets on groove 2 remain as water, though the ice is attempting to reach out in the creation of an in-plane ice bridge, D) a little under 5.5 minutes after the droplets on groove 1 are completely frozen, groove 2 begins to freeze, even though the ice has not bridged the gap between the grooves, additionally, the ice attempting to bridge stops growing without a water source.

Similar freezing mechanisms were observed on the grooved wicks. The grooved wicks began to freeze at 12.5 minutes on average, the most consistent start time of the three surfaces. Once the grooved wick surfaces initiated freezing, the whole observed surface (i.e., the top or portion furthest from the Peltier cooler of the grooves) was frozen, on average, after 8.3 minutes. The droplet diameters at freezing ranged from 24.9 µm–142.7 µm, with an average diameter of 60.5 ± 27.9 µm; the grooved wick had the most consistent droplet diameters (Figure 2.2B). The droplet width is constrained by the width of the grooves (i.e., approximately 86 µm); those droplets which exceed the width of the groove are fewer and grow oblong. The freezing front propagated along individual grooves using ice bridging, similarly to the plain copper surface. However, as shown in Figure 2.4C, ice may attempt to bridge the in-plane distance between two grooves, but it does not cover the distance before the groove begins to freeze (Figure 2.4D). After the second groove freezes, the ice bridge does not continue to grow as it no longer has a water source to draw from. The distance between grooves is greater than the width of the grooves, therefore larger than the majority of the frozen droplet diameters on the grooved wick; the bridging parameter S^* is greater than one. The formation of an ice bridge between droplets on neighboring grooves will not be successful; furthermore, the space between the grooves creates a dry zone that cannot be overcome [8]. This indicates that each groove must initiate freezing and the grooves function as their own independent surface. Since the droplets cannot communicate with droplets on neighboring grooves, the average freezing start time for the observable grooved wick is longer and more inconsistent than the plain copper surface.

The sintered wicks began to freeze at 16.4 minutes, on average. Once the sintered wick surfaces initiated freezing, the entire observed surface was frozen, on average, after 10.9 minutes. The droplet diameters at freezing ranged from 33.9–203.1 µm, with an average diameter of 97.4 ± 32.9 µm (Figure 2.2C). The particles of sintered wicks dictate the location of droplet nucleation and growth. As seen in Figure 2.1, the freezing times for the sintered wick varied from 3.9 to 17.0 minutes; more than and averaged longer than that of the plain copper surface and grooved wick. It was also observed that an increased start time did not result in an increased freezing time. Previous results showed that freezing start times correlate with total time to freezing [42]. This can be explained by the structure of the sintered wick. Due to the nature of sintering, the sintered wick has 'voids', i.e., space without particles. Images of the sintered wick were run through Python image processing code and the percentage of voids to total area was calculated (section 2.3). The amount of void area in an observed area varied due to the randomness of the sintered particles along the wick. As the amount of void area increased, the time it took for the wick to freeze also tended to increase. Decreasing the amount of area for droplets to form limits the number of droplets that can interact with one another. Additionally, decreasing the total area for droplets to form also decreases the size droplets can grow, limiting the distance droplets can transverse to interact with one another. These limits impact the freezing front propagation, increasing the time it takes the surface to freeze. The freezing front must be able to bridge the voids, travel around the voids, or stochastic freezing must occur for the freezing front to continue. While the amount of void area impacts the freezing front, so does the length and width of the void or the occurrence of 'peninsulas' of sintered particles stretching into the void. These can allow for droplets to be close enough to communicate across voids. The freezing front on the sintered wicks is propagated by ice bridging, stochastic freezing of droplets, and cascade freezing.

Ice bridging can only occur on the sintered wick where sintered particles exist such that $S^* < 1$ for the droplets. Figure 2.5A depicts a liquid water droplet whose neighboring droplets have frozen. Figure 2.5B depicts the ice bridges growing from the frozen droplets to the liquid droplet, and Figure 2.5C depicts the ice bridges reaching the liquid droplet and inducing freezing. Due to the location of the sintered particles creating the wick, the distance between the droplets was too large for the freezing front to propagate predominantly by ice bridging. Similar to the grooved wick surface, the sintered wick has multiple locations where $S^* > 1$; the location of the sintered particles creates voids or dry zones between the droplets where droplets cannot form and therefore ice bridging propagation cannot occur. Additionally, due to these dry zone voids, the freezing propagation tends to move from various frame edges towards the center, instead of propagating in one direction, similar to the micropillar surfaces with geometrical defects found in [43].

The sintered wick also froze via stochastic freezing – the water droplets reached freezing conditions (i.e., the Gibbs free energy barrier is overcome [8, 55]), shown in Figure 2.5D-F and depicted in Figure 2.2D. These droplets may overcome the Gibbs free energy barrier due to the roughness and edges of the sintered particles. Figure 2.5D depicts a liquid droplet with some frozen droplets on the sintered particles surrounding it, light is reflected on the droplet. Without any of the neighboring frozen droplets interacting with the liquid droplet, the liquid droplet freezes; the droplet loses reflectance (Figure 2.5E) and transmittance (Figure 2.5F) as it freezes.

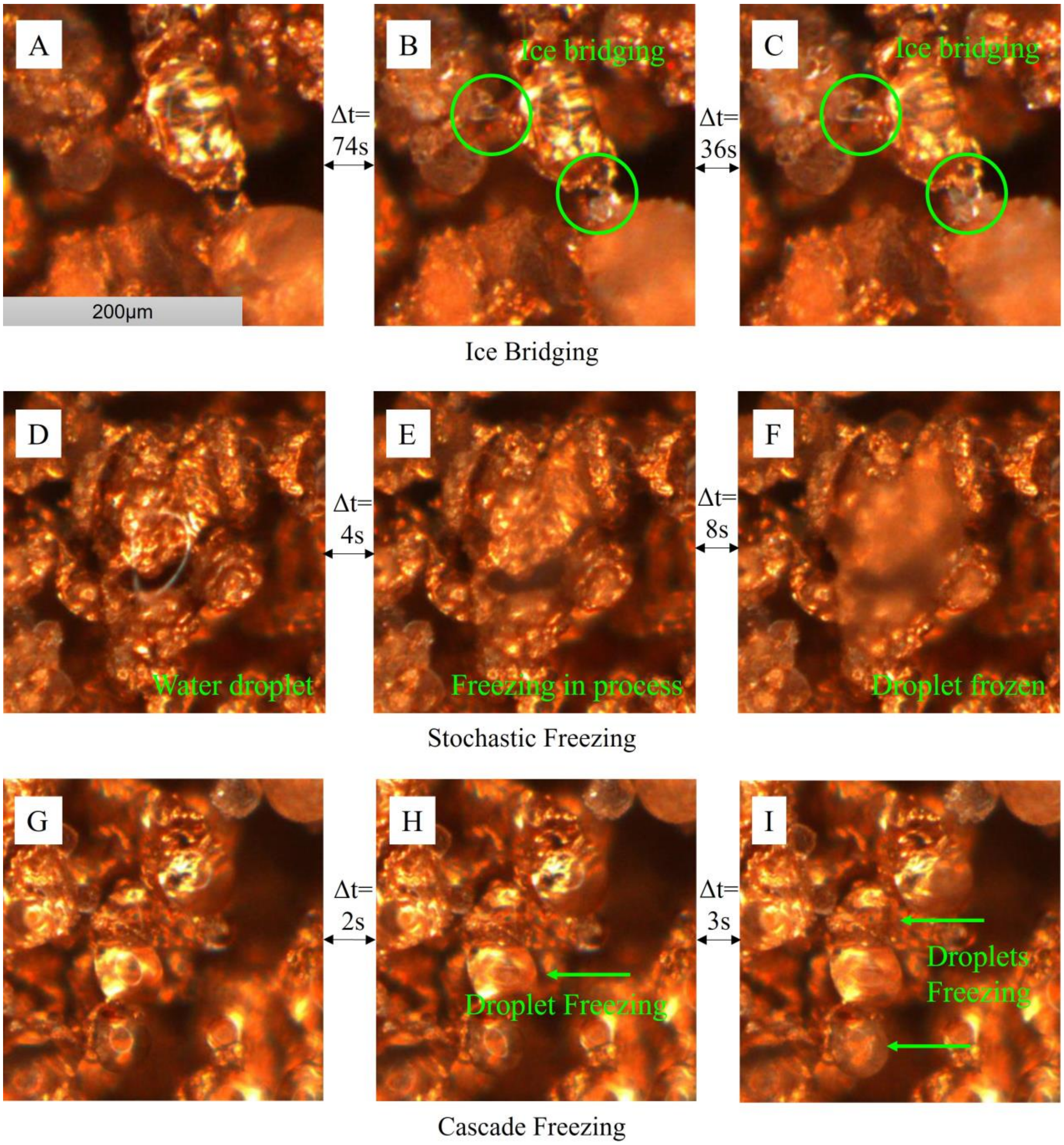

Figure 2.5 The mechanisms of droplets freezing on the sintered wick. (A-C) show ice bridging (supplementary video), (D-F) shows a droplet freezing despite experiencing no interactions from the droplets surrounding it via stochastic freezing; the freezing process is observed by the loss of reflectance between (D) and (E) and loss of transmittance between (E) and (F) (supplementary video), (G-I) show droplets freezing due to cascade freezing; the two additional droplets freeze within a second of the first and are seen in supplementary video

The last method of freezing front propagation along the sintered wick surface is cascade freezing, depicted in Figure 2.2D. A freezing droplet initiates freezing in close neighboring droplets ~less than 1 sec after beginning to freeze; the neighboring droplets begin to freeze following the initial droplet but before an ice bridge would be able to begin forming) (Figure 2.5G-H)[19, 60]. Figure 2.5G depicts a group of three liquid droplets not experiencing any interaction with the surrounding frozen droplets. The middle droplet in Figure 2.5 begins freezing and expels water vapor that impinges on the two neighboring liquid droplets, resulting in the liquid droplets freezing (Figure 2.5I).

Stochastic freezing is not the predominant method of freezing a surface due to the time it takes for droplets to overcome the Gibbs free energy [3, 4, 32, 55-57]. On the observed surfaces, the average freezing start times were 6.3 minutes on the plain, 12.5 minutes on the grooved, and 16.4 minutes on the sintered. The droplets on the observed surface could not overcome the Gibbs free energy before freezing propagation mechanisms reached the observed surface. The freezing began on the edges of the observed surfaces, indicating freezing from interaction with the droplets outside of the observed surface; a droplet in an area of lower Gibbs free energy (e.g. a surface edge) froze allowing propagation to the observed surface [32]. Ice bridging has been observed to propagate swiftly on surfaces, the speed of ice bridging propagation relies on the length of bridges required [3, 7]. Ice bridging on the plain copper surface with close droplets created ice bridges within 4 and 7 seconds in Figure 2.3. Haque et al. [3] correlated the bridge length to bridging time for droplets on graphene surfaces, the longer the bridge the longer it took to bridge the gap, with the lengths between 3 μm and 23 μm and corresponding times between a few seconds and 60 seconds. The average times for the observed surfaces to completely freeze were 4.6 minutes and 8.3 minutes, respectively. Both the plain and grooved surfaces froze primarily via ice bridging. While ice bridging takes a few seconds, cascade freezing occurs within milli- or deci-seconds [19, 60]. The plain surface droplets can interact with each other and freeze via droplet bridging; however, the droplets on one groove cannot interact with the droplets on a neighboring groove. Similarly, due to voids on the sintered surface, there are areas where the droplets cannot interact, slowing the freezing front (section 2.3). On the sintered wick, in the videos corresponding to Figure 2.5G-I, the neighboring droplets are seen experiencing cascade freezing following the freezing of the first droplet. Additionally, the freezing start time and the freezing time are proportional in all three surfaces, similar to results in Bohm et al. [42].

Understanding the freezing mechanisms on wicking surfaces can lead to wick designs that can mitigate the damaging effects of heat pipe freezing. The topography of the surfaces has greater impacts on the freezing time by influencing the freezing mechanisms and the speed at which the freezing front can propagate. The plain copper surface can employ ice bridging across its entire length, with minimal interference. Therefore, a majority of the droplets formed on the surface resulted in a bridging parameter of less than one. While the grooved surfaces employ ice bridging as well ($S^* < 1$), the droplet-to-droplet interaction is restricted to droplets along the same groove. Droplet bridging from the top of one groove to another fails due to the S^*>1, thereby increasing the time for the grooved surface to freeze, as each groove must freeze individually. The sintered surfaces employ a mixture of ice bridging ($S^* < 1$), stochastic freezing, and cascade freezing. The freezing times on the sintered wick were the most varied of the three surfaces, had the most varied freezing start times, as well as the longest freezing start and end times, as a result of the differing area taken up by voids. The varied freezing times result from the dry zone voids ($S^* > 1$) created by the sintered particles and the sintered particles themselves acting as surface defects or edges; additionally, the surface topography results in varied freezing methods of different length and time scales – ice bridging, stochastic freezing, and cascade freezing. This research shows the opportunity for optimization of heat pipe geometry to take advantage of the different time and length scales associated with the different freezing mechanisms to prevent harmful effects of freezing. The void structure and surface energy could be tailored to simultaneously allow for wicking the liquid state but prevent ice bridging and cascade freezing mechanism.

2.2 Experimental apparatus

Three geometries were considered: a copper sintered wick surface (Adv Thermal Solutions, ATSHP-F8L150S45W-455, flat heat pipe, 9.45mm wide), a copper grooved wick surface (Adv Thermal Solutions, ATS-HPD6L300G30W-00, round heat pipe, 6.0mm in diameter), and a plain copper surface. The sintered and grooved wick surfaces were from commercially available heat pipes; the heat pipes were cut in half lengthwise and split into 25-mm-long sections. A trough was cut into a copper block of 25-mm and matching widths of the heat pipes and the heat pipe sections inserted for better control of the temperature across the wick surfaces. Indium thermal interface material was pressed between the heat pipe and trough to ensure good thermal contact. Two different sections of the sintered heat pipe and grooved heat pipe were used. The plain surface was a rectangular 110 copper block (20mm × 25mm × 6.35mm). [61]

The experiments were conducted in an environmental chamber with a temperature set to 22°C and the relative humidity set to 60%, monitored with an Omega OM-24 Data Logger. The heat pipe test section or plain copper surface was clamped onto the Peltier cooler and heat sink, with Arctic Silver Thermal Paste applied between the test surface and Peltier cooler for thermal contact. The surface was placed under the confocal microscope (Leica DVM2500 Digital Microscope) with a set zoom of 50×. Three thermocouples (TMQ316SS-062G-3) along the edge of the copper blocks were inserted to monitor the surface's temperature. Following assembly, water at 5°C was pumped through the Peltier's heat sink (NESLAB RTE-111) and the microscope was used to record video. The Peltier cooler was then set to -5°C. The experiments ran for approximately one-hour, sufficient time for the surfaces to completely freeze [61]. The plain surface, grooved wick 1, grooved wick 2, sintered wick 1, and sintered wick 2 surfaces were observed for five replicates.

Freezing start and end times were determined using image processing and visualization. To aid in the visualization of ice formation, a Python image processing code was developed. The first frame of the video was used as a baseline, in which no condensation or ice formation had occurred, and was subtracted from the subsequent frames. This allowed for deviations from the original frame to be highlighted, thereby making the condensed water and ice formation more visible. The approximate times for freezing to begin and end were determined and the subtracted frames within this time range were recompiled into a video and analyzed visually to determine the freezing start or end time.

2.3 Image analysis of voids in sintered wick

The sintered wicks have voids in plain that disrupt edge-to-edge freezing propagation, unlike the plain copper and grooved wick. There are areas of the wick without any sintered particles, hereafter called voids. These voids occur randomly in the sintered wick surface and can be of varying lengths and widths. These voids affect where condensation can occur, the size of droplets, and the distance between droplets, thereby affecting freezing propagation along the surface.

A Python algorithm was written to determine the percentage of void area in the observed sintered wick areas. To determine the red, green, and blue (RGB) values corresponding to the voids in the sintered wick freezing videos 15 images were cropped to contain only voids and analyzed through Python image processing code. A range for RGB values corresponding to the pixel color values of the voids was output; $15 \leq R \leq 142, 3 \leq G \leq 59, 0 \leq B \leq 31$. Instances of ice bridging the voids were run through the same image processing and output an additional set of RGB values; $145 \leq R \leq 255, 64 \leq G \leq 166, 12 \leq B \leq 123$. Further image processing was then

Table 2.1 Time to freeze sintered wick and corresponding percentage of void area in the sintered wick prior to freezing and condensation and the percent decrease of the void area after freezing has occurred compared to the original void area

	Time to freeze (min)	% of void area prior to freezing	% decrease of void area after freezing
A	3.5	35%	7%
B	4.5	40%	8%
C	5.0	55%	15%
D	5.3	38%	10%
E	8.0	57%	14%

completed. An algorithm was written to evaluate the percentage of pixels consisting of voids in the observed surface before condensation had begun, as well as the percentage of pixels consisting of voids and not ice in the observed surface once freezing was completed. The images were manipulated such that the void area became black ($R = 0$, $G = 0$, $B = 0$) and the sintered particle area became white ($R = 255$, $G = 255$, $B = 255$) and saved as a new image (Figure 2.6). The percentage of void area prior to freezing and condensation and percent decrease of void area after freezing are displayed in Table 2.1 and sorted by increasing time to freeze.

While a higher amount of area taken up by voids tended to increase the amount of time it took for the sintered wick to freeze (e.g. Figure 2.6C has more void space than Figure 2.6A and took 4.5 minutes longer to freeze), it is not the only factor. As seen circled in red, the surface in Figure 2.6C-D had fewer instances of ice bridging across large voids than the surface in Figure 2.6A-B. The surface in Figure 2.6A has more instances where the sides of the large voids are closer together or have 'peninsulas' of sintered particles reaching into the void, decreasing the distances between sides, and thereby decreasing the distance between droplets. Additionally, surface D took longer to freeze, 5.3 minutes to freeze, but had less void area, 38%, than surfaces B and C. Upon inspection of the surfaces, surface D had two large voids blocking the corner where freezing propagation began. These voids increased the freezing time of the observed surface C, the freezing front was not able to cross these voids. The percent decrease of void area after freezing tended to increase as the percent of void area prior to freezing increased; the existence of more voids allowed for more opportunities of, and need for, ice bridges to form over small voids. However, as noted earlier, voids where S^{*}>1 hinders the front propagation.

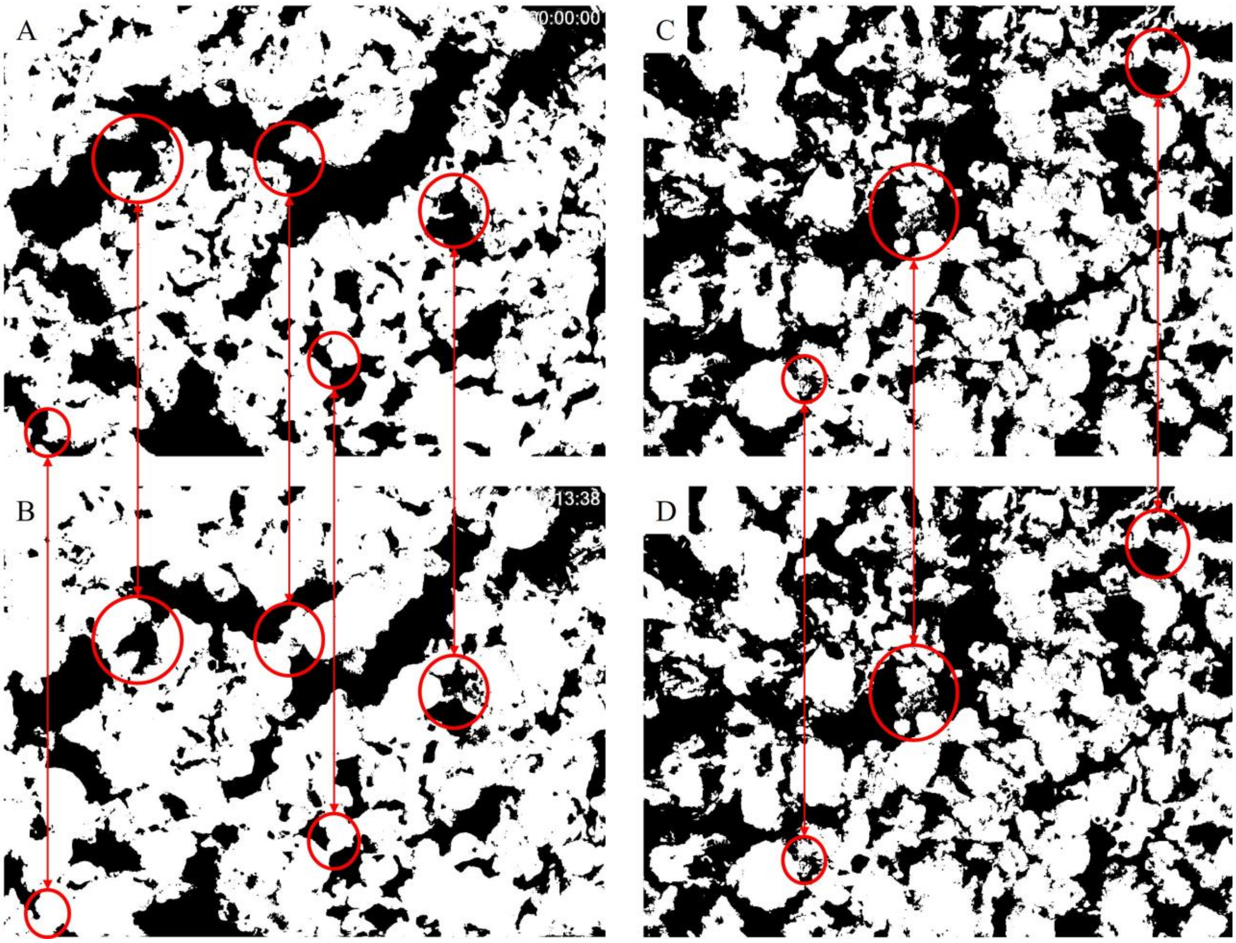

Figure 2.6 Black and white images depicting the voids (black) and sintered particles (white) on two different observed areas (1532 µm×1149 µm) of a sintered wick; (A-B) and (C-D). The red circles indicate mapped locations where ice bridging occurred across voids. (A) an observed sintered wick area before condensation began. The void area is 35% of the total observed area. (A) An observed sintered wick area before condensation began. The void area is 35% of the total observed area. (B) The same area from (A) after freezing in 3.5 minutes. The void area decreased to 28%. (C) An observed sintered wick area before condensation began. The void area is 57% of the total observed area. (D) The same area from (C) after freezing in 8.0 minutes. The void area decreased to 43%.

Chapter 3 - Droplet Spray Literature Review

3.1 Nozzle spray dynamics

Nozzles are used for agricultural applications, such as irrigation and spraying agricultural products (e.g., pesticide); flat fan and cone nozzles are the most commonly used for applying agricultural products [62]. Flat fan sprays apply uniform coverage, while cone nozzles tend to have smaller droplet sizes than fan nozzles [62] and therefore have less variance in droplet size [63]. Sprinkler irrigation systems (e.g., center pivots) are commonly used for irrigation (i.e., used on 55% of crop land in the United States [64]) and are considered a water-saving irrigation technology [9, 64-67]. Low energy precision application (LEPA) bubbler nozzles for sprinkler irrigation have a more precise application of water, allowing for less water-use and LEPA nozzles operate lower to the ground than other sprinkler nozzles, reducing the potential for spray drift [68-72]. Bubbler nozzles work by spraying liquid out of the nozzle orifice in a jet, the jet then hits the bubbler plate and the liquid flows through and around the plate to the ground; it is not sprayed horizontal [72]. Nozzle designs (e.g., geometry, the spray angle for sheet sprays, orifice size, and flow rate) play substantial role in spray dynamics [10, 62-64, 67, 71, 73-82].

Droplet sizes of sprays are categorized into eight different categories via the ASABE S572.1 standard; from smallest to largest droplets, the categories are Extremely Fine (<60 µm), Very Fine (61 – 105 µm), Fine (106 – 235 µm), Medium (236 – 340 µm), Coarse (341 – 403 µm), Very Course (404 – 502 µm), Extremely Coarse (503 – 665 µm), and Ultra Coarse (>665 µm) [10]. Different droplet sizes have pros and cons for various applications (e.g., coarse sprays are used for herbicides [10, 11, 62]). At different operating pressures, a nozzle produces a spray at different velocities and can change the droplet size categorization being produced (e.g., increasing the pressure, thereby increases the velocity of the spray and results in decreased droplet sizes [62-65, 73, 77, 78]).

In an agricultural setting, the size of the droplets is important since smaller droplets provide better coverage overall, but are prone to drift (i.e., the sprayed liquid does not make it to the intended plants or soil). Drift increases water loss in irrigation, thereby increasing the amount of irrigation water needed, and can be environmentally problematic if pesticides are sprayed [62, 74, 76, 77, 83-85]. Additionally, the droplet size can affect the droplets' ability to adhere to plants [11]. Distribution of the droplet sizes is dependent on the nozzle geometry and flow rate of the spray (e.g., increased pressure results in a decreased droplet size and increased velocity [77]), in addition to the surface tension of the water [63, 76, 79, 83, 86, 87]. There are multiple variables governing spray dynamics; what is true for one nozzle is not inherently true for another, and what is true for one spray flow rate is not the same for a different flow rate even within the same nozzle [62, 63, 76, 83, 86].

When water sprays out of a nozzle, water is ejected as a liquid sheet, which subsequently breaks up and forms droplets. Spray sheets break up because of friction with air creating waves. As the waves grow, the sheet ruptures and creates ligaments (i.e., an unstable, narrow band of liquid that is unattached from the sheet) due to surface tension and shear stress between the liquid and the air. The ligaments decrease until droplets are formed [62, 63, 75, 76, 83, 85, 88-92]. If breakup of the spray sheet occurs closer to the nozzle (i.e., where the sheet of spray is thicker), the droplets will be larger than if breakup occurred farther from the nozzle due to the liquid sheet thinning as it moves from the nozzle; as the spray sheet becomes wider, the water pulls from the middle of the sheet to the edges, and thus the sheet thins [62, 63, 75, 77, 85, 93]. Increasing the operating pressure and velocity decreases the thickness of the spray sheet, thereby decreasing the droplet sizes [62, 63, 94]. Kooij et al. [63] tested multiple nozzles (i.e., Teejets 110-02, 110-03, 110-04; Albuz API 110-03 and Albuz ATR 80 cone) under the same pressures, and determined that the breakup distances and droplet size distribution changed based on the nozzle. A majority of droplets formed retain the velocity of the spray sheet [92]. Table 3.1 summarizes the effect of various properties of pure liquids (e.g., water, ethanol) on the sheet thickness, breakup length, droplet size, spray angle, Weber number, and Reynolds number.

Spray properties – breakup length, sheet thickness, droplet size, spray angle – are impacted by the system geometry and the working fluid properties (i.e., surface tension and viscosity [76, 78, 83, 85, 86, 95]). These properties can be related using nondimensional numbers such as the Reynolds number and Weber number. For example, Davanlou et al. [78] observed decreasing the surface tension until it reaches 48 mN/m resulted in decreased droplet diameters at low Reynolds numbers; however, at high Reynolds numbers, the surface tension did not affect droplet size significantly. Reynolds number is given by:

$$Re = \frac{\rho_l U_{sheet} D_h}{\mu_l} \qquad \mathbf{2}$$

where ρ_l is the density of the liquid, U_{sheet} is the sheet velocity, D_h is the hydraylic diameter of the nozzle, and μ_l is the liquid dynamic viscosity [67, 75, 78, 81, 94].

Weber number is given by:

$$We = \frac{\rho_l U_{exit}^2 b}{\sigma} \quad \mathbf{3}$$

where ρ_l is the density of the liquid, σ is the surface tension, U_{exit} is the liquid velocity at the nozzle exit, , and b is the characteristic length (minor axis of the elliptical opening of the flat fan nozzle), $b^2 \sim A_{hyd}$, A_{hyd} is the hydraulic area [63, 83, 94, 96]. The Weber number is inversely impacted by surface tension. When the surface tension is decreased, the Weber number is increased [78, 95]; The Weber number can also be increased by an increase in velocity of the spray (achieved by increasing the pressure) [94]. The Weber number can then be used to determine the droplet diameter [63, 83]:

$$d = Cb\alpha^{-\frac{1}{6}} We^{-\frac{1}{3}} \quad \mathbf{4}$$

where C is a dimensionless constant, and $\alpha = \rho_{air}/\rho_{liquid}$ is the density ratio.

Table 3.1 The impacts of increasing and decreasing various properties in pure liquids impacts other spray properties in fan and cone nozzles - sheet thickness, breakup length, droplet size, spray angle, Weber number, and Reynolds number. When a surfactant is used to alter surface tension, the effect of surface tension deviates from the table.

	Sheet thickness	Breakup length	Droplet size	Spray angle	Weber number	Reynolds Number
↑ Nozzle Orifice Diameter	↑ [62, 79, 80]	↑ [62, 74, 79, 81, 97, 98]	↑ [62, 64, 97, 99, 100]	N/A [74]	↑ [63, 67, 83, 94, 96]	↑ [67, 75, 78, 81, 94]
↑ pressure/ spray velocity	↓ [62, 80]	↓ [67, 75, 81, 93, 94, 101-103]	↓ [62-64, 73, 74, 77, 78, 97, 99, 100, 104]	↑ [78, 79, 81, 93]	↑ [63, 67, 78, 82, 83, 94, 96, 105]	↑ [67, 75, 77, 78, 81, 82, 94]
↑ sheet thickness		↑ [106, 107]	↑ [62, 63, 75, 77, 85, 100, 108, 109]	N/A	N/A	N/A
↑ Breakup length	N/A		↓ [63, 74, 75, 77, 83, 85]	N/A	N/A	N/A

↑ Spray angle	↓ [100, 110]	↓ [111]	↓ [74, 100, 110]		N/A	N/A
↓ Surface Tension	N/A	↓ [78, 86, 95]	↓ [62, 73, 76, 78, 86, 93]	↑ [78, 101, 112]	↑ [63, 78, 83, 94-96]	↓ [77, 78]
↑ Viscosity	↑ [80]	↑ [101]	↑ [62, 78, 93, 108, 113] *Re Dependent*	↑ [78]	↑ [78]	↓ [67, 75, 78, 81, 94]
↑ Weber number	↑ [80]	↓ [63, 75, 89, 97, 102, 114]	↓ [63, 78, 83, 94, 97]	↑ [112]		
↑ Reynolds number	N/A	↓ [81, 97]	↓ [81, 97, 104]	↑ [78-81]		

3.2 Agricultural applications of surfactants

The addition of surfactant alters the surface tension of water, thereby changing spray dynamics. The use of surfactants has been investigated in soils to alter the soil-water interactions in an effort to maintain water content in the soils [50, 115-118]. Lehrsch et al. [115] sprayed surfactant directly onto three soils and irrigated; they measured an increase in water retention in the larger soil pores (i.e., greater than 15 µm) compared to the control of pure water, but runoff and erosion were not affected. Dekker et al. [119] observed that surfactant-treated soil was wetter after rain events; however, the distribution below the soil was uneven and had larger differences in maximum and minimum soil water content than the untreated soil. The uneven wetting could be affected by the depth the surfactant penetrated. Fernández-Gálvez and Mingorance [116] observed for silty loam soil from Spain, changing the wetting contact angles via surfactant affects the soil wetting characteristics. Gutierrez et al. [50] determined the addition of Surfactin to sandy loam and loam soil at a lab scale increased the constant evaporation rate while decreasing the slower evaporation rate allowing water to remain in the soil for longer when water was scarce.

Surfactants are also used in various agricultural spray products to alter spray by increasing spray stability and altering droplet sizes to improve the performance of the agricultural spray [62, 83]. Since surfactants decrease surface tension, they also increase the wettability of sprayed droplets on leaves (i.e., spreading on leaves), which is of benefit since it allows plants to be affected by the agricultural spray [83, 120]. Additionally, since surfactants alter the properties of the spray, the spray dynamics can change (e.g., breakup, droplet size) [73, 76, 83, 84, 86, 93, 95]. Surfactant solutions alter spray dynamics similarly to pure liquids, as shown in Table 3.1; however, decreasing the surface tension via surfactant has an inconsistent effect on breakup length and droplet size (sections 3.3.4 and 3.4) [73, 83, 84, 86, 95]. Surfactant solutions produce a time-dependent, dynamic surface tension; it begins near the surface tension of the bulk liquid (e.g., water) and decreases as it moves further from the nozzle and the surface age increases [76, 83, 95, 121-124]. This dynamic surface tension results from the surfactants movement to the newly created interface and absorption to said surface [76, 83, 122-125]. When breakup occurs, new surfaces are created and surfactant has to diffuse to these edges and absorb to the interface [62, 83, 122, 123]. For example, Sijs and Bonn [76] observed that the dynamic surface tension for different adjuvants varied from 70 mN/m at the youngest surface age to 20 mN/m at the oldest surface.

3.3 Spray Sheet Breakup

3.3.1 Wavelength and aerodynamic waves

Four atomization regimes exist for jets (Figure 3.1): Rayleigh (at lower velocities with droplets larger than the spray orifice; the droplets form via capillary pinching at the end of the jet), first wind-induced (air impacts breakup resulting in droplets of similar size to the spray orifice), second wind-induced (unstable wavelengths drive breakup into droplets smaller than the spray orifice), and atomization (droplets are immediately stripped off the jet or sheet when exiting the orifice at high velocities, resulting in droplets up to two orders of magnitude smaller than the orifice) [110, 114, 126].

Rayleigh breakup regime is driven by surface tension forces and is characterized by droplets comparable to or larger than the jet stream [82, 114, 127, 128]. The Rayleigh breakup occurs multiple diameters of the nozzle orifice away from the nozzle and the breakup length of the jet has been characterized based on the jet diameter as approximately [114, 129, 130]

$$L_b \cong 1.89 * d_{jet} \quad \mathbf{5}$$

The Rayleigh breakup length has also been modeled on spray parameters [82, 131],

$$L_b = 19.5 d_{jet} We^{0.5}(1 + 3Oh)^{0.85} \quad \textbf{6}$$

First wind breakup regime occurs due to surface tension forces with the additional aid of aerodynamic forces and is characterized by droplets similar in diameter to the jet diameter with breakup occurring many nozzle diameters downstream [82, 114, 130].

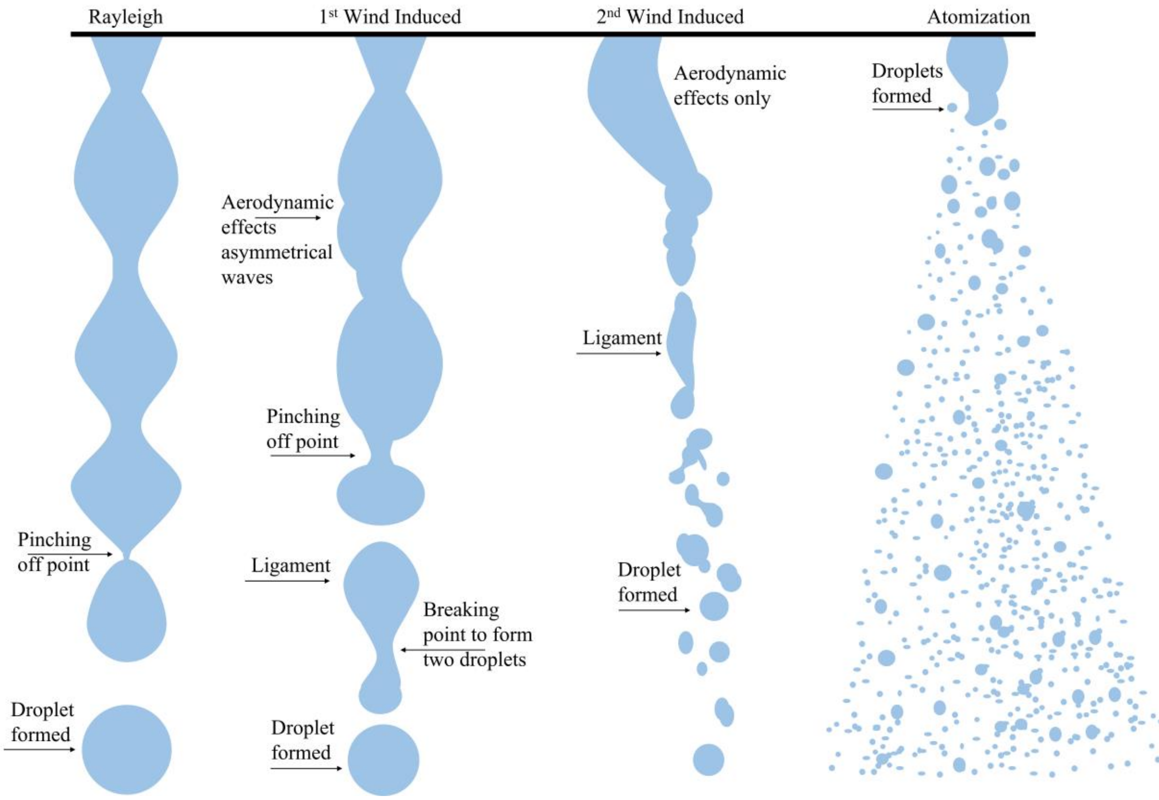

Figure 3.1 The four methods of breakup into droplets. Rayleigh breakup is dominated by surface tension forces where droplets are pinched off the end of the jet, the droplets are the same diameter or larger than the jet diameter. 1st wind induced breakup is still driven by surface tension force but with the addition of aerodynamic forces, the droplets formed are similar in size to the jet diameter. 2nd wind induced breakup is dominated by aerodynamic forces on the jet and results in droplets smaller than the jet diameter or nozzle orifice. Atomization occurs at the nozzle exit and results in droplets much smaller than the nozzle orifice.

Most agricultural spray nozzles fall within the second wind-induced breakup regime [110]. Aerodynamic waves, commonly in the transverse direction, form in spray sheets and jets, resulting in the disintegration or breakup of the sheet or jet into ligaments and are considered to be the dominant mechanism of breakup in irrigation spray nozzles [63, 75, 80, 81, 83, 86, 92, 93, 110, 113]. The waves reach a critical amplitude, breaking the sheet at crests and troughs when reaching a critical amplitude, which is assumed to be equal to the sheet thickness with help from surface tension forces [75, 86, 88, 102, 108]. The waves result from the interaction of the liquid with the air, i.e., shear instabilities and surface tension [93, 108, 109].

The waves are not consistent through the whole sheet [83]; however, for pure liquids, the fastest growing wavelength in a fan sheet (i.e., the wavelength responsible for breakup) is given by [86, 92, 110]:

$$\lambda_{crit} = \frac{4\pi\sigma}{\rho_{air} U_{sheet}^2} \quad \mathbf{7}$$

where σ is a constant surface tension, ρ_{air} is the air density, and U_{sheet} is the sheet velocity. For pure liquids, the wavelength decreases with a lower surface tension [86]. The diameter of ligaments formed via short waves and long waves can be determined by [89, 110, 132]:

$$d_{lig,short} = \sqrt{16h/K_s} \quad \mathbf{8}$$

$$d_{lig,long} = \sqrt{8h/K_s}$$

where h is the half sheet thickness, K_s is the is the wave number corresponding to maximum wave growth rate. For short waves, K_s is determined by maximizing the growth rate equation [89, 110, 132]:

$$\omega = -2U_{sheet}k^2 + \sqrt{4U_{sheet}^2 k^4 + \frac{\rho_{air}}{\rho_l} U_{sheet}^2 k^2 - \frac{\sigma k^3}{\rho_l}} \quad \mathbf{9}$$

where U_{sheet} is the liquid velocity, k is the wave number. For long waves [89, 110, 132]:

$$K_s = \rho_{air} U^2/(2\sigma) \quad \mathbf{10}$$

Ligaments break up when the wave's amplitude is larger than the radius of the ligament [113]. The diameter of the formed droplet can then be determined by [89, 110]

$$d_{droplet} = 1.88 d_{lig}(1 + 3Oh)^{1/6} \quad \mathbf{11}$$

where Oh is the Ohnesorge number and defined as $Oh = \mu_l/(\rho_l \sigma d_l)^{\frac{1}{2}}$. The Ohnesorge number compares the viscous forces to the inertial and surface tension forces.

Surface-active agents, such as surfactants, are inconsequential to the development of the spray close to the nozzle. They only affect where the spray is not rapidly changing (i.e., at a newly created surface the surface tension is equal to the pure solvent due to the dynamic surface tension [76, 83, 95, 110]). However, surfactants can alter the wavelength of the spray sheet [86]; for example, Sijis et al. [83] found that the addition of AOT decreased the wavelength by 1.2 mm.

3.3.2 Formation of holes in spray sheets

Perforations, or holes, can occur in the spray sheet due to turbulence in the nozzle before being sprayed [101]. They tend to occur towards the center of the sheet towards the bottom [75, 92]. Perforations grow due to surface tension forces until they reach another hole [75, 92, 101, 113]. Droplets can form at the collision of two holes; a bridge forms where the holes merge and eventually pinches off from the overall sheet in two symmetric points. This forms a ligament that either contracts into a single droplet or breaks apart further into droplets [109, 133]. Holes move at the same velocity as the sheet [75, 92].

Unwettable, hydrophobic particles in the spray can also cause the formation of holes; wettable particles do not affect the spray dynamics [101]. The addition of emulsion droplets (e.g., oil) in sprays creates surface tension gradients leading to Marangoni stresses, causing the sheet to thin and rupture, thereby creating holes [75]. Bag breakup can also form holes within the spray sheet; aerodynamic waves within the spray shift from experiencing drag to pressure, and the air pressure expands the point on the sheet into a bag until it bursts and forms droplets [75]. Bag breakup occurs more at lower operating pressures [94].

The growth rate of a hole is given for the minor and major diameters as [75]:

$$growth\ rate\ D_{minor} = \sqrt{\frac{2\sigma}{\rho h}} \tag{12}$$

$$growth\ rate\ D_{major} = \frac{U_{sheet} D_{major_0}}{l_0} + 2\sqrt{\frac{2\sigma}{\rho h}}$$

where σ is the surface tension, ρ is density, h is the half thickness of the sheet, U_{sheet} is the magnitude of the sheet velocity, D_{major_0} is the initial major diameter of the hole, and l_0 is the initial distance of the hole from the nozzle. Breakup length is not affected by hole formation and growth; while more holes appear at higher pressures, the velocity of the spray is too high for them to grow significantly [75].

3.3.3 Edge breakup

The amount of breakup along the edge depends on the design of the nozzle, operating pressure, and liquid characteristics [113]. Ford and Furmidge [113] observed edge ligaments forming between $250 < Re < 300$. In a flat fan nozzle, ligaments form at the edges of the spray sheet and break into larger droplets than those formed at the center of the sheet [92, 94, 113]. Breakup of the sheet edge is independent of break up within the sheet and creates larger droplets [113].

3.3.4 Variables changing the breakup length

The length of the spray sheet at breakup (i.e., breakup length) is a determining factor for droplet size; the longer the sheet, the smaller the droplets [62, 63, 75, 77, 83, 85]. This is due to the spreading out, and therefore thinning, of the sheet [63]. The farther the distance from the nozzle, the thinner the sheet becomes, thereby reducing the potential volume of a droplet after breakup. The breakup length is measured from the nozzle to the point in the spray at which there is a continuous void across the sheet. The sheet thickness is dependent on the nozzle orifice diameter, the size of the orifice determines the amount of liquid that can exit the nozzle; as the diameter is increased the sheet thickness increases [62, 79, 80]. The sheet thickness has an inverse relationship with operating pressure [62, 80] and an inverse relationship with the spray angle [100, 110]. Increasing the spray angle will decrease the sheet thickness due to a larger area for the water to cover [100, 110]. Dexter [93] observed the addition of surfactants did not significantly affect the sheet thickness.

The size of the nozzle opening indirectly affects the breakup length by directly impacting mass flow rate. If a nozzle exit is larger, a larger mass flow rate may exit, thereby increasing the breakup length [62, 79]. The increased volume of water increases the time it takes for the sheet to become thin enough to break up. Increasing the velocity of the spray is most often achieved by increasing the operating pressure. The increase in pressure and spray velocity results in a decreased breakup length; the increased velocity results in earlier holes in the spray sheet [75]. The spray sheet is more susceptible to initial disturbances that can cause breakup at lower velocities than at higher velocities [75].

Increasing the viscosity will reduce the effects of the aerodynamic forces, thereby increasing the breakup length of the spray [101]. Theoretically, decreasing the surface tension will decrease the breakup length of a spray; this has been observed for pure liquids (e.g., ethanol), as shown in Table 3.1 [78, 86, 95]. However, the addition of surfactant resulting in a decreased surface tension has provided mixed results of decreased and increased breakup lengths [73, 76, 83, 86]. Various increases in breakup length have been observed from approximately 1 mm to 20 mm depending on the surfactant, concentration, nozzle, and pressure [73, 76, 83, 86]. Additionally, breakup lengths were also observed to decrease by similar amounts with the addition of surfactant (Table 3.2) [73].

Breakup length is inversely related to the Weber number due to the relation of the Weber number to the wavelengths; the higher the Weber number, the shorter the breakup length [63, 75, 80, 114]. The gas Weber number ($We_g = \rho_g V^2 h/\sigma$) indicates a transition from long to short wavelength regimes ($We_{g,crit} = 27/16$) [75, 80, 89]. Aerodynamic-wave-dominated breakup (section 3.3.1) can be modeled as [75, 89]:

$$L_b = \begin{cases} U_{sheet}\left[3\ln\left(\frac{\eta_b}{\eta_0}\right)\right]^{\frac{2}{3}}\left(\frac{J\sigma}{(\rho_{gas}/\rho_l)^2 U_{rel}\rho_l}\right), & We_g < \frac{27}{16} \\ \frac{U_{sheet}}{\Omega_s}\ln\left(\frac{\eta_b}{\eta_0}\right), & We_g > \frac{27}{16} \end{cases} \quad \textbf{13}$$

where U is the velocity of the sheet, U_{rel} is the velocity of the sheet relative to the ambient gas, $\ln\left(\frac{\eta_b}{\eta_0}\right)$ is experimentally determined, J is a constant, Ω_s is the maximum growth rate of the wave (eq. 9 $\omega = \Omega_s$).

The surfactant's effects on spray dynamics depends on the surfactant, the nozzle, and the flow rate [62, 63, 73, 76, 83, 84, 86, 95]. Much of previous research has focused on surfactants and adjuvants added to agricultural sprays, such as pesticides. Butler Ellis et al. [86] investigated sheet breakup from two flat fan nozzles at 2.5 bar and a disc and core hollow nozzle at 3 bar with various surfactants]test surfactants: Fatty alcohol ethoxylate (C10), Fatty alcohol ethoxylate (C17), Polyoxyethylene sorbitan fatty acid ester, Alkoxylated ethylenediamine, and Alkyl polyglycoside) resulting in different surface tensions at breakup (27.2 mN/m, 44.6 mN/m, 41.9 mN/m, 48.8 mN/m, and 26.4 mN/m, compared to pure water at 69.9 mN/m). They saw varied increased breakup lengths (e.g., sheet lengths from 31 to 44 mm) with the addition of surfactant compared to pure water due, in part, to decreased surface tension.

Sijs and Bonn [76] investigated spray droplet sizes from flat fan and conical nozzles between 1 and 5 bars with several commercially available adjuvants (Addit, Agral Gold, Break Thru S240, Silwet Gold, Synergen, Wetcit, and Zipper) with different surface tensions (equilibrium surface tension: 26.4 mN/m, 25.8 mN/m, 21.6 mN/m, 21.3 mN/m, 29.1 mN/m, 33.5, mN/m, and 21.8 mN/m). Decreasing the surface tension decreased the breakup length (in line with studies of pure liquids summarized in Table 3.1, but counter to the Butler Ellis et al. [86]) and the mechanism of droplet breakup for a spray with surfactant was qualitatively the same as that for pure water. However, Kooij et al. [63] observed spray breakup with lowered surface tensions to be more unstable. The surfactant's effect on the breakup length of the liquid sheet depends on the surfactant; in addition to differing surface tensions, the diffusion rate of surfactant through the liquid may affect the thickness of the sheet and thereby affect the oscillations [86]. The surfactant altered the oscillations causing sheet breakup, thereby altering the formation of ligaments and droplets [86].

Table 3.2 Effect of various surfactants on breakup length and how much surfactant increases the breakup length compared to pure water

First Author, Year	Surfactant	σ (mN/m)	Nozzle	Breakup length (mm)	Surfactant breakup – pure water breakup (mm)
Sijs 2021 [83]	AOT	$\sigma_{eq} = 25.8$		32.5 ± 0.6	1.7
Butler Ellis 1999 [73]	Ethokem	$\sigma_{eq} = 68$	Standard	38	5
			Pre-Orifice	30	7
			Hollow Cone	22	8
			Evenspray	44	10
			Low Pressure	60	20
	Agral	$\sigma_{eq} = 25.8$	Standard	34	1
			Pre-Orifice	28	5
			Hollow Cone	15	1
			Evenspray	38	4
			Low Pressure	45	5
	Li-700	$\sigma_{eq} = 52$	Standard	23	-10
			Pre-Orifice	12	-11
			Evenspray	24	-10
			Low Pressure	30	-10
Shavit 1995 [95]	Tergitol NP-10	57	Air assist atomizer	23	0
		44		26	3
		37		24	1
		34		22	-1

3.3.5 Numerical modeling of breakup

Numerical models of spray breakup from jets typically assume the flow through the nozzle is turbulent and use k-epsilon (k-ε) model to simulate said flow, along with the volume of fluid (VOF) method accounting for the conservation of mass and momentum equations. In the VOF method, the spray field is split into cells, these cells can contain either water, air, or a combination of both – this is accounted for via a concentration variable, α, where $\alpha = 0$ indicates air, $\alpha = 1$ indicates water, and $0 < \alpha < 1$ indicates a mixture of air and water [77, 79]. Nadeem et al. [77] compared manual numerical calculations to particle image velocimetry (PIV) measured experiments and found the results for jet velocity matched within ±1% error. The numerical model can also provide the velocity distribution.

Breakup has been modeled for spray sheets using software such as CFD library OpenFOAM v1812 with the Navier-Stokes equations governing the simulation [75]. Asgarian et al. [75] observed similar patterns of simulated spray breakup to the experimental breakup and hypothesized that the differences were due in part to the modeling of the nozzle geometry, as the geometry greatly affected the spray. Neglecting surface disturbances resulted in the simulated breakup length (20 mm) being shorter than the experimental (24.7 mm). OpenFOAM can also simulate the spray via VOF and large-eddy simulation (LES) methods; it simulated wave amplitudes and the formation of ligaments in primary breakup [87]. Lucchini et al. [132] modeled gasoline spray using eqs. 8, 9, 10, 11, 13 and an evaporation equation in OpenFOAM to accurately model gasoline spray sheet thickness at breakup and droplet size, while Nadeem et al. [77] utilized CFD software ANSYS and modeled spray from a nozzle based in k-ε and VOF modeling. A fine mesh (56741 nodes) was used to model the spray and compared to PIV experimental measurements, CFD modeling was within ±5% error.

3.4 Droplet size

The geometry of a nozzle orifice impacts the size of the droplets formed [62, 64, 99, 100]; the nozzle orifice size dictates the size of the spray (i.e., the mass flow rate through the nozzle and the spray angle), thereby affecting sprayed droplet sizes [62]. Additionally, for breakup occurring within the second-wind regime, droplets will be smaller than the nozzle orifice [110, 114, 126].

The increase of operating pressure increases the velocity of the spray, and, decreases the droplet size (eq. 4) [62-64, 73, 74, 77, 78, 97, 99, 100, 104]. For one Polysirbate spray solution, Davanlou et al. [78] tested pressures of 10, 15, and 20 bar and observed average droplet sizes of

27, 25, and 23 µm respectively. Butler Ellis and Tuck [73] observed greater decreases of droplet size with pressure; from 1 bar to 4 bar there was consistently a decrease of around 100 µm.

The thinning of the sheet decreases the droplet size, as the available liquid to form ligaments, and then droplets, decreases [62, 63, 75, 77, 85, 100, 108, 109]. As sheet thickness is related to the breakup length, as the breakup length increases, the sheet thickness decreases and so do the droplet sizes [63, 74, 75, 77, 83, 85]. For example, Sijs et al. [83] added AOT surfactant to water; compared to water, the AOT solution increased the breakup length 1.7 mm and decreased the droplet size by 10 µm.

As the spray angle increases, the droplet size decreases [74, 100, 110]. This is due to the spreading of the sheet creating a thinner sheet thickness, thereby decreasing the amount of liquid available to form droplets [74, 100, 110]. Additionally, increasing the spray angle can decrease the droplet distribution [100].

When solving for the median droplet diameter using eq. 4, where eq. 3 is used for the Weber number, it is seen that the droplet diameter is directly proportional to the surface tension. If the surface tension is decreased, the droplet diameter decreases (Table 3.1) [62, 73, 76, 78, 86, 93]. However, this relationship does not always hold true when the surface tension is reduced via surfactant [62, 73, 83, 86]. To solve for mean droplet size, the average droplet size equation (eq. 4) can be used with the dynamic surface tension at the characteristic length instead of the equilibrium surface tension [63, 83].

Butler Ellis et al. [86] decreased the spray surface tension with the addition of surfactant Fatty alcohol ethoxylate (C10; $\sigma = 51 \pm 1.5$ mN/m at breakup) and reduced the volumetric median droplet diameter (D_{V50}) by 28 µm. The volumetric median diameter is based on the 3D droplet size, it is explained further and determined using eq. 16. When a propan-1-ol, a pure liquid, was added ($\sigma = 50.5 \pm 0.5$ mN/m at breakup) the droplet size was reduced only by 9 µm [86]. Therefore, surface tension is not always a perfect predictor of droplet size, and other properties are likely affecting droplet sizes [86]. The same surfactant or additive has also been observed to either increase or decrease the droplet size depending on the nozzle type or pressure [73].

Sijis et al. [83] observed an average droplet size of 157 ± 4 µm water with the addition of AOT surfactant, a 10 µm decrease compared to water. The AOT surfactant had no significant effect on the shape of the droplet size distribution only decreasing the average droplet size. While AOT does decrease the average droplet size, it does not have as great an impact as lowering the surface tension with ethanol, a pure liquid [83]. When applied to the average droplet size equation, the equilibrium surface tension of the surfactant-water mixture does not adequately predict the droplet size, instead, the equation must use the dynamic surface tension [83]. It is of interest to note in Dexter's study [93] the surfactants considered insoluble increased the droplet size compared to water, while the soluble surfactants decreased the droplet size.

Viscosity has a larger effect on short wave breakup than on long wave breakup [62]. The effect of viscosity on droplet size can also depend on the nozzle [62] (i.e., viscosity also affects the droplet size more in smaller nozzles than in larger nozzles [113]). At higher operating pressures (10 bar), increasing the viscosity will increase the droplet size, and at lower and medium (5-10 bar) pressures will not affect it [78, 113]. While the viscosity alters the average droplet diameter, it does not affect the droplet size distribution significantly [113]. Part of the inconsistent effect could result from the increase of viscosity stabilizing the edge rim of sheets where larger droplets typically form but also increasing the formation of holes [111].

3.5 Spray angle

The spray angle of a nozzle is built into the design; however, changing properties can alter the angle to a degree [62, 74, 105]. When the operating pressure is increased, more liquid is attempting to exit the nozzle orifice thereby increasing the spray angle [78, 79, 81, 93]. The spray angle can also be increased by decreasing the surface tension, the decreased surface tensions allows the spray to spread easier [78, 101, 112]. Davanlou et al. [78] investigated three different surface tension liquids (60, 48, and 30 mN/n) that resulted in spray angles of 52°, 62°, and 68° respectively at 7 bar with the same nozzle. Davanlou et al. [78] also investigated water and two different viscosity liquids, and found increasing the viscosity will increase the spray angle when the operating pressure is under 15 bar. A higher Reynolds number will have a larger spray angle; however, a Reynolds number (Re = 21,000) will be reached at which the spray angle will no longer increase [81]. The spray angle has been correlated to be proportional to the Weber number by Son et al. [112]. The proportion differed depending on operating pressure.

3.6 Nondimensional numbers in sprays

The Reynolds number (relates inertial and viscous forces) can be increased by increasing the nozzle diameter (eq. 2) [67, 75, 78, 81, 94], increasing the pressure [67, 75, 77, 78, 81, 94], increasing the surface tension [78], or decreasing viscosity [67, 75, 78, 81, 94]. When the spray has a low Reynolds number, the droplet diameter is affected by surface tension and the flow is laminar, however at high Reynolds numbers, surface tension plays less of a role and inertia plays a greater role and the flow is turbulent [77, 78]. When the Reynolds number is higher, the droplet size will decrease; increasing the Reynolds number decreases the breakup length [81, 97, 104].

The Weber number (relates inertial and surface tension forces) can be increased by increasing the nozzle diameter [63, 67, 83, 94, 96], increasing the operating pressure (eq. 3) [63, 67, 78, 83, 94, 96, 105], decreasing the surface tension (eq. 3) [63, 78, 83, 94-96], or increasing the viscosity [78]. Sijis and Bonn [76] determined that using the dynamic surface tension at a characteristic time of about 20 ms was appropriate to determine the Weber number of surfactant spray, thereby accurately predicting the mean droplet size and droplet size distribution – depending on the nozzle and pressure. When the Weber number is higher, the droplet size will be smaller [63, 78, 83, 94, 97]; this is directly seen in the average droplet size diameter in eq. 4.

3.7 Gaps and Objectives

Altering the surface tension in a spray fluid changes the breakup length and the droplet size. If the surface tension is decreased by using a pure liquid, the breakup length decreases as well as the droplet sizes; however, if a surfactant is used, the results vary depending on the nozzle and the surfactant used. A majority of the literature investigating the use of surfactants on spray dynamics focused on the fan and cone nozzles, as surfactants are commonly used in these for crop coverage purposes, and thus there is limited research investigating surfactants in alternative nozzles, such as the bubbler nozzle. The objectives of this dissertation are to investigate how the addition of Surfactin to sprayed water affects the spray dynamics (the breakup length, the spray angle, and droplet size) under various nozzle applications (flat fan nozzle, full and hollow cone nozzles, bubbler nozzle) and operating pressures.

Chapter 4 - Experimental Apparatus

4.1 Experimental apparatus

An experimental apparatus was designed and built to evaluate the effects of Surfactin (SurfPro Surfactin, CAS # 302933-83-1) on spray dynamics of different irrigation nozzles for a range of pressures (Figure 4.1). The Surfactin solution was 0.1% concentration Surfactin by weight added to distilled water (section 4.2). The fluid (i.e., distilled water or 0.1% Surfactin solution) is pulled from a water tank via a pump. A bypass loop directly followed the pump, and a pressure relief valve was directly before the Coriolis flow meter to ensure the operating pressure did not exceed the upper limit of the nozzles. A Coriolis flow meter (Emerson model F025S319CCAAEZZZR/2700I12BBAEZZZ) was used to measure the mass flow rate, a thermocouple (TMQ316SS-062G-3) recorded the temperature of the spray prior to entering the nozzle in LabVIEW, and an absolute pressure transducer (PX309-200A5V) recorded the pressure of the spray entering the nozzle in LabVIEW. The spray was collected and returned to the tank using a pump. The ambient pressure (PX409-100G5V) was recorded in LabVIEW to obtain the gage operating pressure of the nozzle. The ambient temperature and relative humidity (Omega OM-24 Data Logger) were also measured.

The fluid was sprayed into ambient air where a Fastec IL5 camera captured images of the spray in FasMotion. An LED high speed photo flash (Vela One) was used to backlight the image,

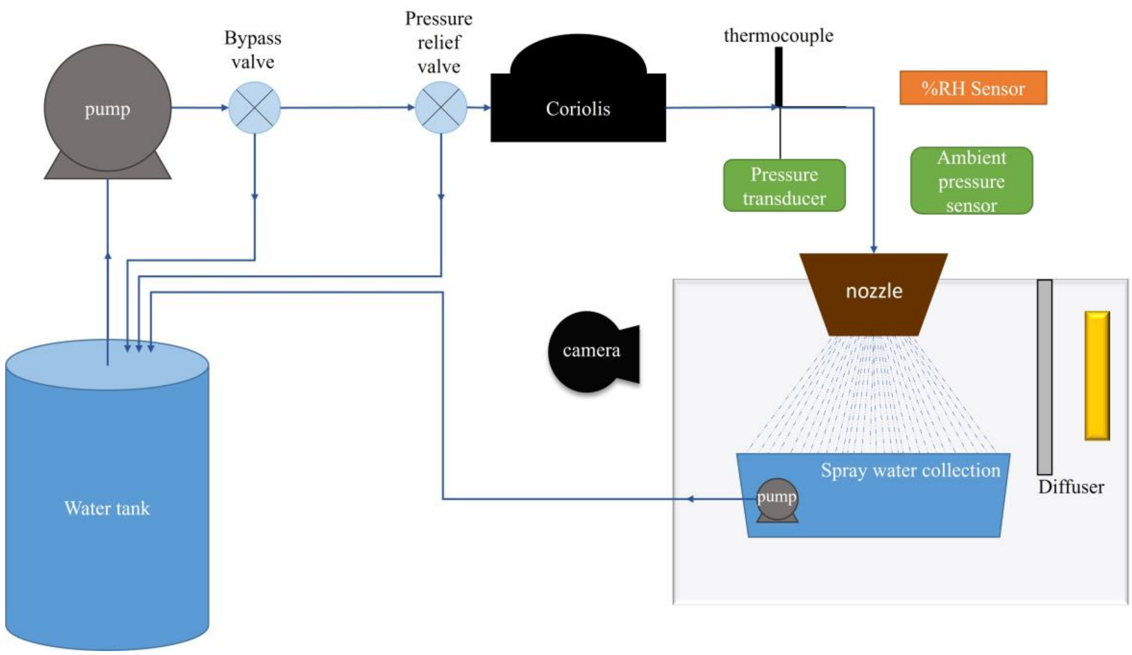

Figure 4.1 Diagram of the spray apparatus

the light was diffused using ground glass against the light and white fabric between the light and the spray. The flash was set to a pulse length of 5 µs, with burst strobe count of 4 with an interval of 250 µs. The flash was connected to the camera via a trigger (Miops Camera Trigger, UPC 791154017609). Twenty images of each nozzle at each operating pressure were taken.

Three different types of nozzle spray were investigated at various operating pressures. Four TeeJet fan nozzles (DG11005VS, DG110015VS, DG9505EVS, DG95015EVS) were investigated at pressures of 30, 45, and 60 psi (206.8, 310.3, and 413.7 kPa). Two flat fan nozzles (i.e., DG11005VS and DG110015VS) were designed for spray angles of 110°, while the other two flat fan nozzles (i.e., DG9505EVS and DG95015EVS) were designed for spray angles of 95°. Of the flat fan nozzles, DG110015VS and DG95015EVS were designed for a flow rate of 0.5 GPM (0.031545 L/s) at 40 psi, and DG11005VS and DG9505EVS were designed for 0.15 GPM (0.0094635 L/s) at 40 psi. One TeeJet full cone nozzle (TG-3) was investigated at 20, 30, 45, and 60 psi (137.9, 206.8, 310.3, and 413.7 kPa). This nozzle was designed for a flow rate of 0.3 GPM (0.018927 L/s) at 40 psi. Bubbler nozzles were investigated at 6, 10, and 15 psi (41.4, 68.9, and 103.4 kPa). Two Senninger Pressure-Master Regulator Medium-Flow for 6 and 15 psi and one Nelson Pressure Regulator for 10 psi, a bubbler pad was attached to the end of the nozzle.

Table 4.1 Nozzles investigated

Label	Nozzle Part Number	Nozzle Spray Type	Flow rate at 40 psi (GPM)	Spray Angle	Test Pressure (psi)
F1	TeeJet DG95015	Flat Fan	0.15	95°	30, 45, 60
F2	TeeJet DG110015	Flat Fan	0.15	110°	30, 45, 60
F3	TeeJet DG9505	Flat Fan	0.5	95°	30, 45, 60
F4	TeeJet DG11005	Flat Fan	0.5	110°	30, 45, 60
C	TeeJet TG-3	Full Cone	0.3	N/A	20, 30, 45, 60
B6	6 psi	LEPA Bubbler		N/A	6
B10	10 psi	LEPA Bubbler		N/A	10
B15	15 psi	LEPA Bubbler		N/A	15

4.2 Surfactin mixture

Various concentrations by weight were mixed and surface tension data were acquired by Augustine Scientific. Surface tension measurements were recorded at 20°C by the Wilhelmy plate method, ASTM1331; the surface tensions are shown in Table 4.2. The difference in surface tension between 0.08% and 0.1% concentration was minimal, indicating that increasing the concentration results in negligible decrease in surface tension; 0.1% concentration was selected due to the surface tension value of 29.2 mN/m and for ease of mixing. An initial 15 L of solution was mixed; 7.5 g of Surfactin were slowly added to 1 L of distilled water while being mixed by a magnetic mixer at 800 RPM. Once completely mixed, it was added to the tank. A second liter was mixed with the same method, with 7.5 g of Surfactin. 13 L of pure distilled water were then added to the tank.

Table 4.2 Surface tension of Surfactin solutions by weight, data obtained by Augustine Scientific

Sample	Surface Tension
Pure Water	72.79 ± 0.01 mN/m
0.005% Concentration	66.38 ± 0.01 mN/m
0.010% Concentration	47.67 ± 0.02 mN/m
0.030% Concentration	30.95 ± 0.01 mN/m
0.050% Concentration	30.06 ± 0.01 mN/m
0.080% Concentration	29.41 ± 0.01 mN/m
0.100% Concentration	29.20 ± 0.02 mN/m

4.3 Data analysis

ImageJ was used to determine the droplet sizes in the spray images. The images were processed in ImageJ: despeckle (a median filter) was used, the contrast was enhanced 0.3% saturated pixels, find edges was used, and the image was converted to black and white using the "make binary" function. The ImageJ binary function "close" was used to close semi circles and unfilled-in droplets. Droplet areas were then obtained using the ImageJ "Analyze Particles" function; an upper boundary (5,500,000 μm^2) was used to exclude the intact sheet and spray ligaments, and the results were saved as a .csv file. The droplet area was used to determine the area equivalent diameter of the droplet using eq. 14. The files were then run through a Python code to determine the droplet volumetric median diameter (D_{V50}) of each image and circularity bins of

0.1 in size for each nozzle and pressure. The volumetric median diameter is the median diameter of the droplets, based on the median droplet volume. The D_{V50} of each image was determined by:

1. Using the area of each droplet in ImageJ to determine the diameter of each droplet:

$$d_i = \sqrt{\frac{4A_i}{\pi}} \tag{14}$$

where d is the droplet diameter, A is the droplet area, and i is the droplet index [134, 135].

2. The volume of each droplet was determined [135]

$$V_i = \pi d_i^{3/6} \tag{15}$$

3. The median volume of the droplets in the image is found and used to determine the D_{V50}:

$$D_{V50} = \left(\frac{6V_{median}}{\pi}\right)^{1/3} \tag{16}$$

where V_{median} is the median droplet diameter.

The circularity was determined by ImageJ using the equation:

$$4\pi \frac{[Area]_i}{[Perimeter]_i^2} \tag{17}$$

A value of 1 indicates a perfect circle and approaching 0 is an elongated shape.

The breakup length was determined using ImageJ's straight line tool; a line was drawn to measure the distance from the center of the nozzle to the point where there were no connections (e.g., ligaments) to the spray sheet. The spray angle was measured using the ImageJ angle tool; the angle of each edge of the spray and the top of the nozzle was marked, measured, and used to determine the spray angle (Figure 4.2).

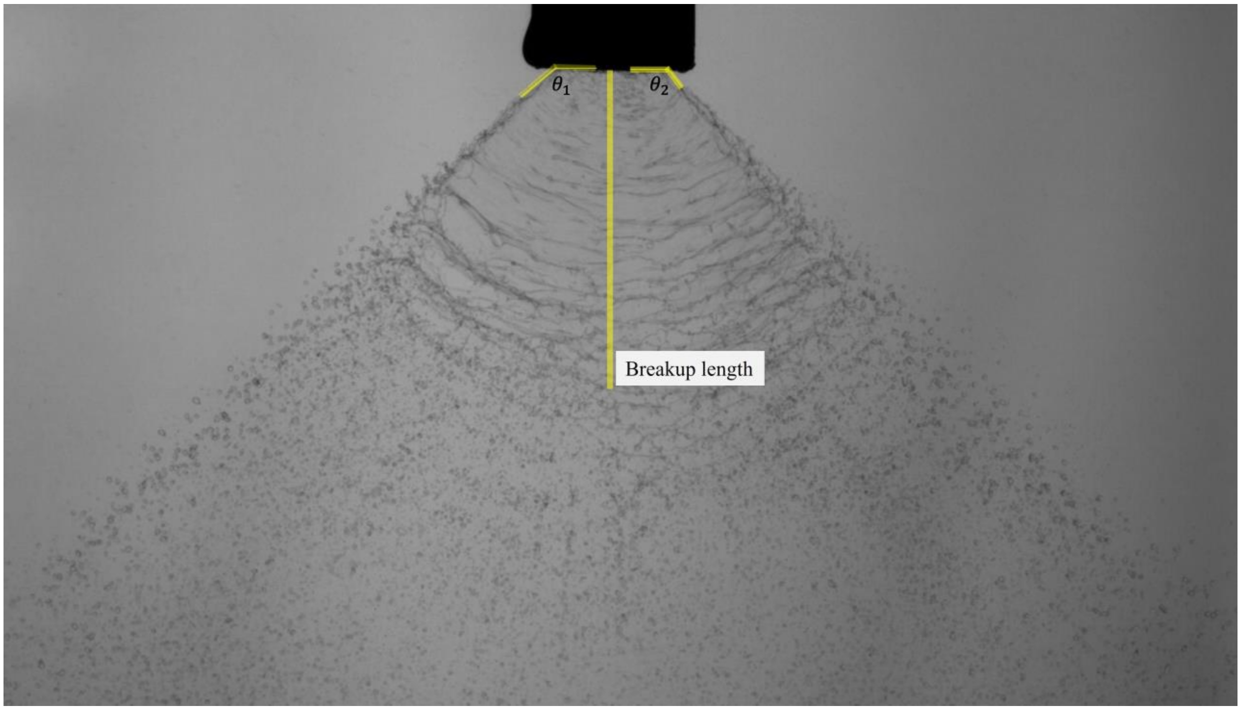

Figure 4.2 Image of flat fan (F1) spray at 30 psi using ImageJ to measure the breakup length and the two angles of he spray sheet edges with the nozzle. The breakup length is 24.328 µm, $\theta_1 = 136°$ and $\theta_2 = 131°$ resulting in a spray angle of $87°$

4.4 Uncertainty

The uncertainty for the pressure measurements is ± 0.26%. The uncertainty of temperature measurements was ± 0.02°C. The relative humidity uncertainty was ± 1% relative humidity. The uncertainty of the mass flow rate was ± 0.05% of the reading.

The uncertainty in the breakup length for the fan and bubbler measurements is two pixels size; ± 90 µm for the fan nozzles, and ± 0.094 mm for the bubbler nozzles breakup length and ligament diameter. The uncertainty for the cone nozzle breakup length was greater due to visual uncertainty; ± 1.5 mm. The uncertainty for the spray angle for the fan and cone nozzle was 2°.

The uncertainty for the droplet diameter in the fan and cone nozzles is one pixel; ±45 µm. The uncertainty for the droplet diameter in the bubbler nozzle increases with pressure due to imaging complications capturing the larger droplets as the velocity increased. For the 6 psi bubbler nozzle the uncertainty for the droplet size is ±0.2 mm, for the 10 psi and 15 psi bubbler nozzle the uncertainty is ±0.5 mm.

Chapter 5 - Results and Discussion

The results and discussion are presented for the effect of surfactant on the breakup length, spray angle, and droplet size in the fan and cone nozzles and the effect of surfactant on the breakup length, jet or ligament diameter, and droplet size in the bubbler nozzle.

5.1 Surfactant's effects in fan and cone nozzles

Spray breakup from the fan (Figure 5.1) and cone (Figure 5.2) nozzles is consistent with the breakup mechanisms for second wind induced breakup. Breakup happens downstream of the nozzle and creates droplets smaller than the nozzle orifice diameter and the waves resulting in breakup are visible [75, 82, 88, 108, 114, 130]. Additionally, increasing the spray pressure results in a decrease in breakup length in the fan (for F1 increasing the pressure from 30 psi to 60 psi

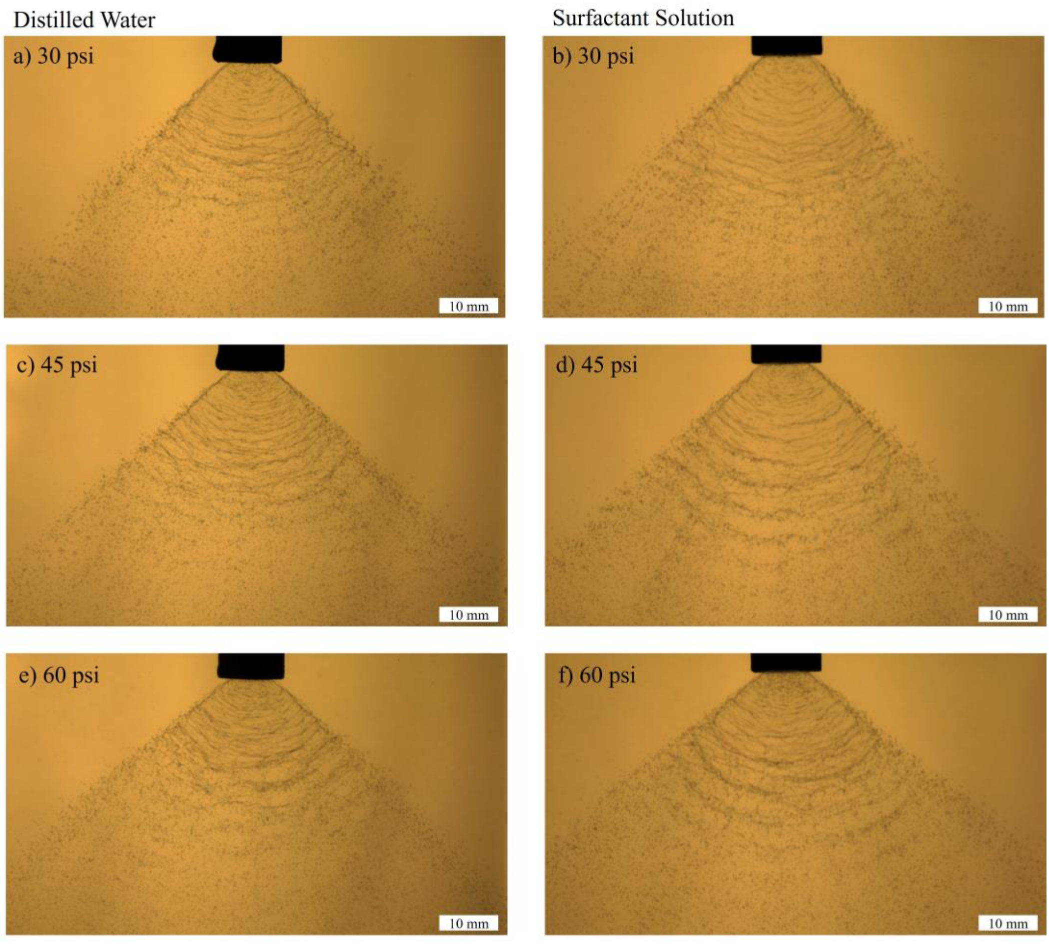

Figure 5.1 Spray images from the F1 nozzle a) distilled water at 30 psi with a D_{V50} = 194.8 µm and L_b = 25.5 mm, b) surfactant solution at 30 psi with a D_{V50} = 133.8 µm and L_b = 26.0 mm, c) distilled water at 45 psi with a D_{V50} = 179.2 µm and L_b = 24.0 mm, d) surfactant solution at 45 psi with a D_{V50} = 133.8 µm and L_b = of 26.1 mm, e) distilled water at 60 psi with a D_{V50} = 137.8 µm and L_b =21.9 mm, f) surfactant solution at 60 psi with a D_{V50} = 123.9 µm and L_b = 23.7 mm

resulted in an 11% decrease in breakup length for distilled water) and cone nozzles (increasing the pressure from 20 psi to 60 psi resulted in an 15% decrease in breakup length for distilled water) for both the distilled spray and the surfactant solution spray (Table 5.1); the breakup length for second wind induced breakup is inversely proportional to the spray velocity [98].

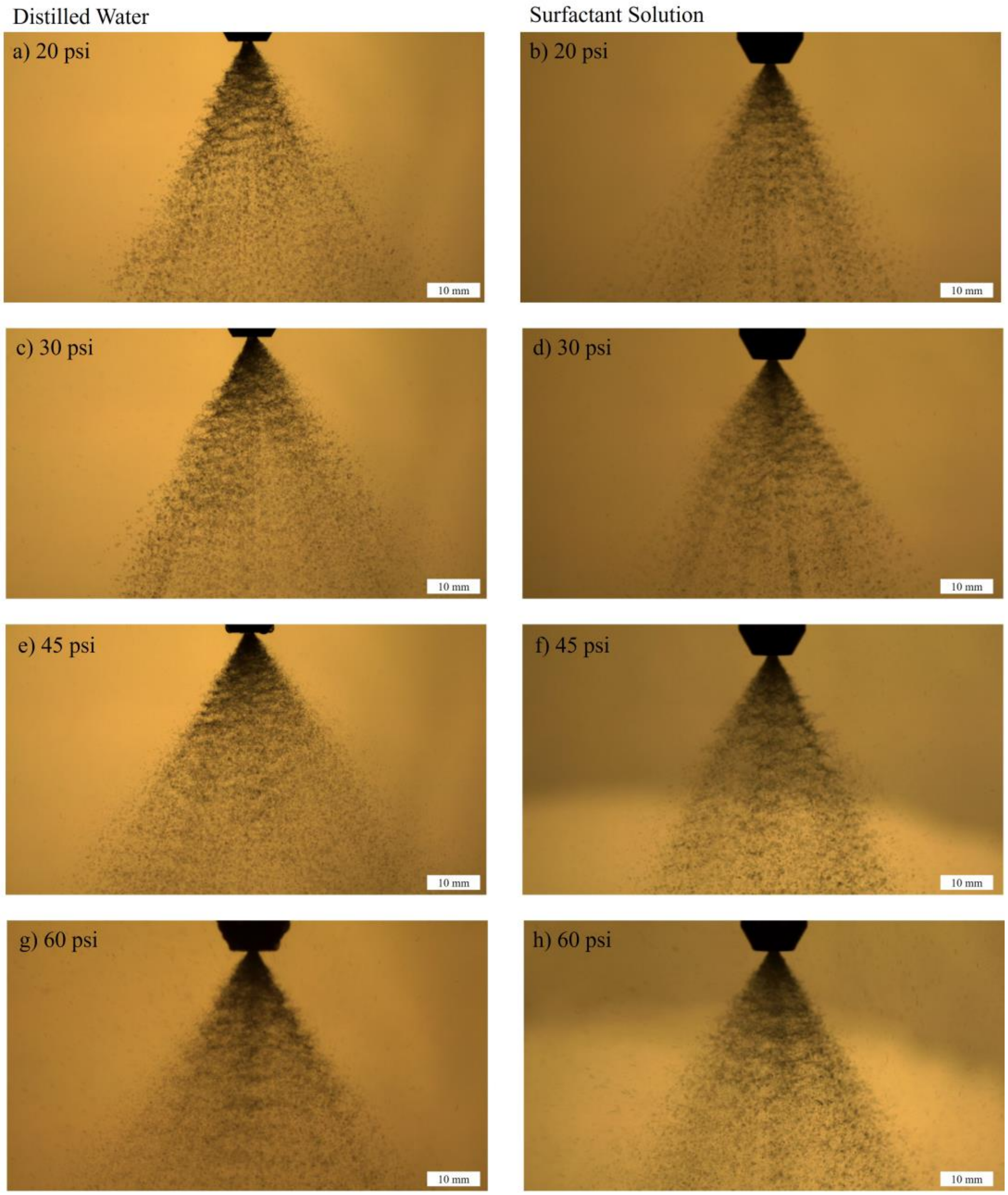

Figure 5.2 Spray images from the cone nozzle (C), a) distilled water at 20 psi with a D_{V50} = 142.2 µm and L_b = 18.3 mm, b) surfactant solution at 20 psi with a D_{V50} = 119.2 µm and L_b = 19.3 mm, c) distilled water at 30 psi with a D_{V50} = 131.6 µm and L_b =15.4 mm, d) surfactant solution at 30 psi with a D_{V50} = 119.2 µm and L_b = 19.4 mm, e) distilled water at 45 psi with a D_{V50} = 131.9 µm and a L_b = 15.6 mm, f) surfactant solution at 45 psi with a D_{V50} = 130.5 µm and L_b = 18.6 mm, g) distilled water at 60 psi with a D_{V50} = 119.1 µm and L_b = 15.5 mm, h) surfactant solution at 60 psi with a D_{V50} of 130.5 µm and a breakup length of 18.0 mm

5.1.1 Surfactant's effects on breakup length and spray angle in fan and cone nozzles

Contrary to pure liquids (Table 3.1) [78, 86, 95], the decreased surface tension of the surfactant solution does not decrease the breakup length of the spray from the fan nozzle; it instead increases it in conjunction with previous research showing that some surfactants increase the breakup length (Figure 5.3 and Table 5.1) (e.g.,) [73, 83, 84, 86]. For the F1 nozzle at 30, 45, and 60 psi, the average breakup length increases by 1.3, 2.6, and 1.4 mm. For the F2 nozzle at 30, 45, and 60 psi, the average breakup length increases by 2, 3.2, and 1.7 mm. For the F3 nozzle at 30, 45, and 60 psi, the average breakup length increases by 11.4, 7.6, and 5.5 mm. For the F4 nozzle at 30, 45, and 60 psi, the average breakup length increases by 2.8, 3.0, and 4.3 mm. The fan nozzle length increases by between 5% and 48%. The breakup length at 45 psi may be the most affected by the surfactant due to being considered a transition in droplet size categories by the manufacturer (i.e., at 45 psi, the F1 and F2 nozzles are transitioning from medium to fine droplets and the F3 and F4 nozzles are transitioning from coarse to medium droplets). For the C nozzle at 30, 45, and 60 psi, the average breakup length increases by 1.2, 4.3, 2.7, and 2.7 mm. The breakup length of the cone nozzle increases by between 6% 28%.

Theoretical modeling of the breakup length results in a proportional dependence of the breakup length on the surface tension of the fluid as well as the wavelength of the spray [98, 136],

$$L_b = 2.5 \ln\left(\frac{a}{c}\right) \sigma \sqrt{\frac{\rho_l}{\rho_{air}^3}} \frac{1}{U_{jet}^2} \qquad \textbf{18}$$

where $ln\left(\frac{a}{c}\right)$ is the initial disturbance factor, σ is the surface tension, ρ_l and ρ_{air} are the density of the liquid and air, respectively, and U_{jet} is the velocity of the jet. While the equilibrium surface tension of the fluid is decreased due to surfactant, the spray experiences a dynamic surface tension (section 3.2). The creation of this surface tension gradient creates Marangoni stresses, which slows the acceleration of the sheet compared to distilled water [136-138]. Additionally, as discussed in 3.3.1, the surfactant can decrease the wavelength, change the amplitude, and reduce growth rate instabilities in the spray sheet thereby affecting breakup [86, 136]. This decrease in conjunction with the dynamic surface tension within the sheet can instead result in the increased breakup length.

Increasing the pressure in the fan and cone nozzles results in a slight increase in the spray angle of the fan nozzles and a negligible decrease in the cone nozzle spray angle. The addition of surfactant to the spray decreases the spray angle (Figure 5.4). In the F1 nozzle at 30, 45, and 60 psi, the spray angle decreases by 3°, 2°, and 1°, respectively; the surfactant decreases the spray angle less at a higher pressure. In the F2 nozzle at 30, 45, and 60 psi, the spray angle increases by 5°, 2°, and 2°. In the F3 nozzle at 30, 45, and 60 psi, the spray angle decreases by 1°, 2°, and increased by 4°. In the F4 nozzle at 30, 45, and 60 psi, the spray angle increases by 3°, 2°, and 3°. In the C nozzle at 20, 30, 45, and 60 psi, the spray angle decreases by 3°, 8°, 1°, and 4°. The averages for the distilled water spray and the surfactant solution spray fall within the standard deviations for each other.

Table 5.1 Breakup length of the fan and cone nozzles at various operating pressures under different spray conditions

Nozzle	Pressure	Distilled spray breakup length (mm)	Surfactant solution spray breakup length (mm)
F1	30 psi (206.8 kPa)	25.4	26.7
F1	45 psi (310.3 kPa)	23.7	26.3
F1	60 psi (413.7kPa)	22.6	24.0
F2	30 psi (206.8 kPa)	24.3	26.3
F2	45 psi (310.3 kPa)	23.3	26.5
F2	60 psi (413.7 kPa)	22.1	23.8
F3	30 psi (206.8 kPa)	23.6	35.0
F3	45 psi (310.3 kPa)	22.7	30.3
F3	60 psi (413.7 kPa)	22.1	27.6
F4	30 psi (206.8 kPa)	25.3	28.1
F4	45 psi (310.3 kPa)	21.0	24.0
F4	60 psi (413.7 kPa)	18.7	23.0
C	20 psi (137.9 kPa)	18.1	19.3
C	30 psi (206.8 kPa)	15.4	19.7
C	45 psi (310.3 kPa)	15.3	18.0
C	60 psi (413.7 kPa)	15.3	18.0

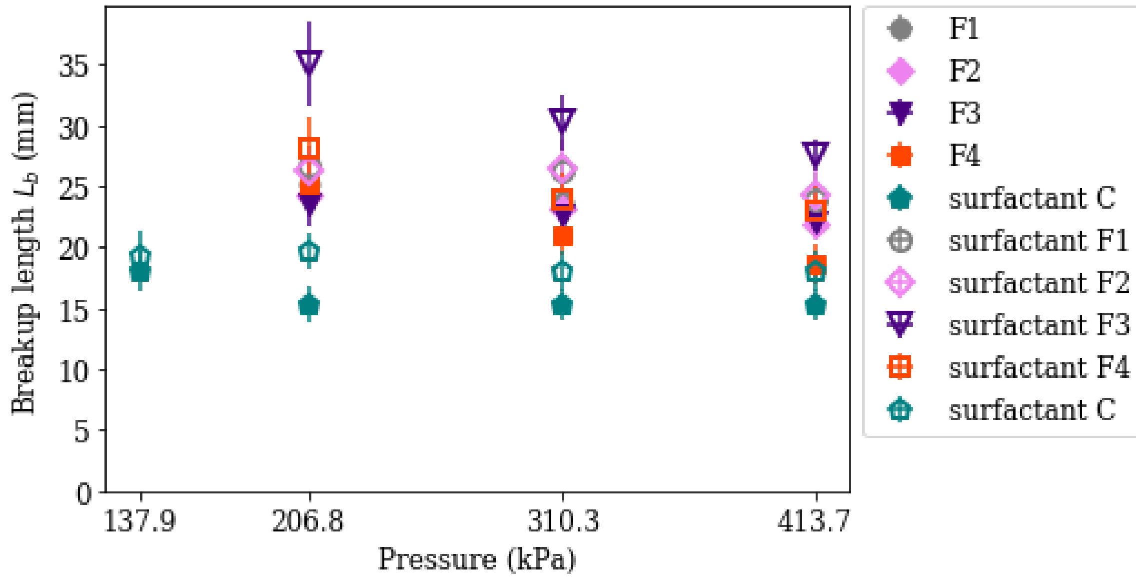

Figure 5.3 Graph of the average breakup length for the fan and cone nozzles with distilled water spray and surfactant solution spray

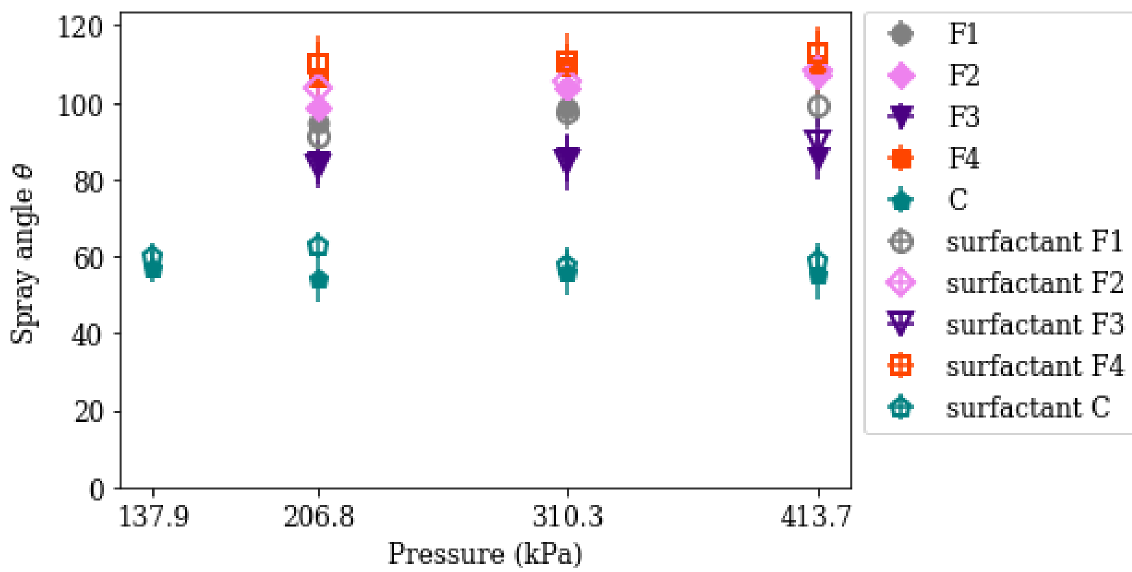

Figure 5.4 Graph of the average spray angle for the fan and cone nozzles with distilled water spray and surfactant solution spray

5.1.2 Surfactant's effects on droplet size in fan and cone nozzles

The droplet size of the fan and cone nozzles tends to decrease as the pressure was increased (Table 5.2 and Figure 5.5), consistent with literature [62-64, 73, 74, 77, 78, 97, 99, 100, 104]. The addition of Surfactin to the distilled water decreases the volumetric median droplet size (D_{V50}) of the fan nozzles (Table 5.2 and Figure 5.5). For each fan nozzle, the surfactant solution's largest

D_{V50} (i.e., lowest operating pressure) has a smaller D_{V50} than the smallest distilled water D_{V50} (i.e., the highest operating pressure); for example in the F1 nozzle, the smallest D_{V50} from the distilled spray is 157.9 µm at 60 psi while the largest D_{V50} for the surfactant spray is less at 134.6 µm at 30 psi. The F1 nozzle is affected the most, as it has both the smallest flow rate as well as the smallest spray angle potentially allowing for more surfactant to exist in the droplets, thereby making breakup into smaller droplets easier. For the F1 nozzle, the surfactant solution decreases the D_{V50} in the F1 nozzle by 65.6 µm (33%), 53 µm (29%), and 26.3 µm (17%) at 30, 45, and 60 psi, respectively. The surfactant solution decreases the D_{V50} in the F2 nozzle by 30.3 µm (17%), 38 µm (24%), and 49.5 µm (31%) at 30, 45, and 60 psi, respectively. The surfactant solution decreases the D_{V50} in the F3 nozzle by 38.1 µm (23%), 42.2 µm (25%), and 44.9 µm (28%) at 30, 45, and 60 psi, respectively. The surfactant solution decreases the D_{V50} in the F4 nozzle by 50.7 µm (30%), 15.3 µm (10%), and 5.4 µm (4%) at 30, 45, and 60 psi, respectively. In addition to the surfactant decreasing the D_{V50} of the fan nozzles, it decreases the variability of D_{V50} across instances (Figure 5.6). The surfactant solution decreases the D_{V50} in the C nozzle by 27.8 µm (19%), 14.3 µm (10%), and 13.4 µm (9%) at 20. 30, and 45, respectively; the D_{V50} increases by 131.1 µm (23%). The full cone nozzle has more droplets forming than the fan due to the more 3D cone shape compared to the flat fan; this can therefore allow more droplet interactions and coalescence and droplet interaction with the spray sheet creating breakup in areas not observed. As the spray sheet moves from the nozzle it becomes thinner, thereby decreasing the size of the droplets [62, 63, 74, 75, 77, 83, 85, 100, 108, 109]. It is also worth noting that that range of D_{V50} decreases with the addition of the surfactant (Figure 5.6).

The droplet size was modeled by Fraser et al. [92] by,

$$d = 3.78\left(\frac{\lambda h}{2\pi}\right)^{\frac{1}{2}} \qquad \textbf{19}$$

where λ is the wavelength and was measured experimentally and h is the sheet thickness, given by $h = \frac{A_{nozzle}}{L_b\theta}$ [93], where A_{nozzle} is the area of the nozzle and θ is the spray angle in radians. The 0.15 gpm nozzles (F1 and F2) wavelengths were observed between 1.2 mm and 3 mm for distilled water and between 1.3 mm and 4.4 mm for the surfactant solution. The 0.5 gpm nozzles (F3 and F4) wavelengths were observed between 1.5 mm and 4.4 mm for distilled water and between 2.0 and 6.0 mm for the surfactant solution. For the distilled water, this model predicts the droplet size depending on the wave length that is experienced; however, for the surfactant solution, the model over predicts the droplet size. For example, none of the surfactant droplets for the F1 and F2 nozzles which experienced a wavelength of 4 mm interacts with the $\lambda = 4mm$ line (Figure 5.7). This is due to the equilibrium surface tension being used, instead a dynamic surface tension needs to be determined.

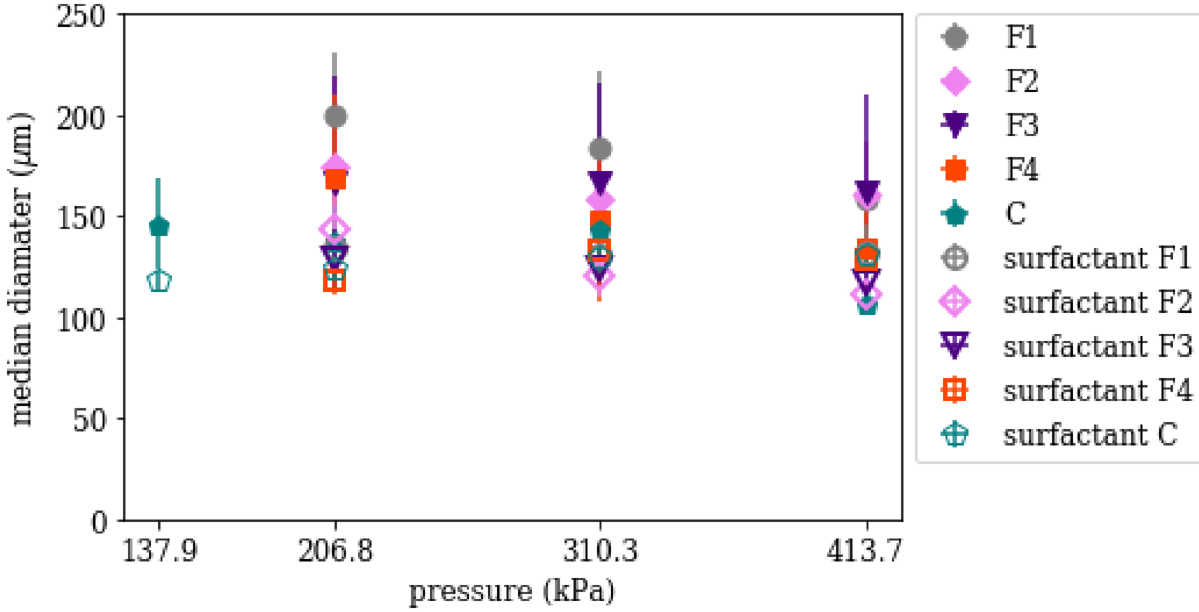

Figure 5.5 Graph of the median droplet size for different nozzles and spray conditions (pressures and spray solution) based on twenty images.

The droplets formed in the fan and cone nozzles tend to be very circular (Figure 5.8). Circularity is measured from 0 to 1, with 0 being the most elongated and least circular shape and 1 being a perfect circle (eq. 17). The distribution of circularity for the surfactant solution was comparable to the distilled water's circularity distribution. While the smaller droplets have are anywhere from 0 to 1, the larger droplets tend to be elongated, i.e., closer to 0 (Figure 5.9).

Table 5.2 Volumetric median droplet diameter of the nozzles at various operating pressures under different spray conditions

Nozzle	Pressure	Distilled Spray Volumetric Median Droplet Diameter (μm)	Surfactant Solution Spray Volumetric Median Droplet Diameter (μm)
F1	30 psi (206.8 kPa)	200.2	134.6
F1	45 psi (310.3 kPa)	183.7	130.7
F1	60 psi (413.7kPa)	157.9	131.6
F2	30 psi (206.8 kPa)	174.3	144.0
F2	45 psi (310.3 kPa)	157.9	119.9
F2	60 psi (413.7 kPa)	160.9	111.4
F3	30 psi (206.8 kPa)	166.6	128.5
F3	45 psi (310.3 kPa)	165.7	123.5
F3	60 psi (413.7 kPa)	161.6	116.7
F4	30 psi (206.8 kPa)	169.0	118.3
F4	45 psi (310.3 kPa)	147.7	132.4
F4	60 psi (413.7 kPa)	134.0	128.6
C	20 psi (137.9 kPa)	146.3	118.5
C	30 psi (206.8 kPa)	138.0	123.7
C	45 psi (310.3 kPa)	143.2	129.8
C	60 psi (413.7 kPa)	106.8	131.1

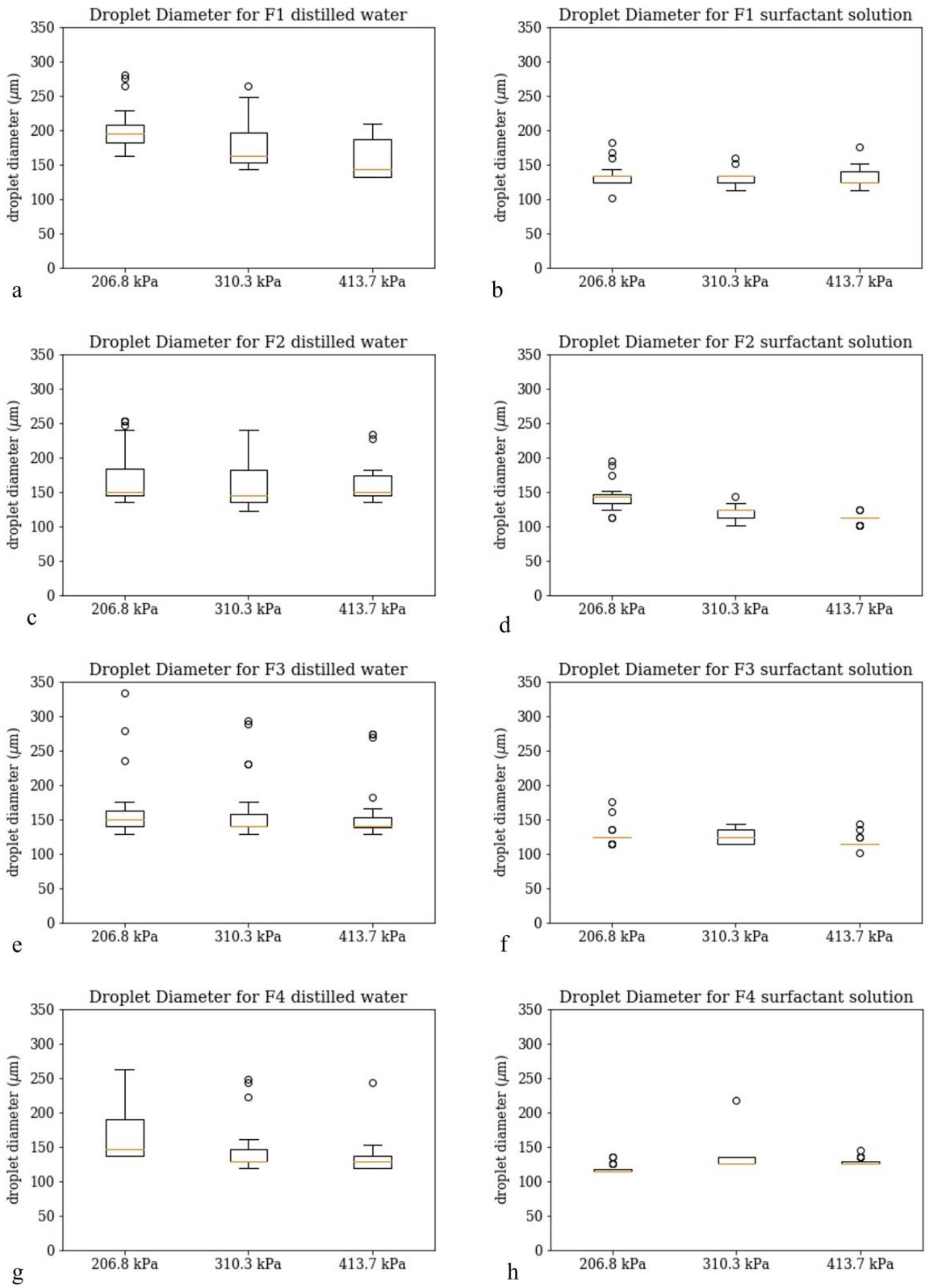

Figure 5.6 Box and whisker plots of the median droplet diameters for the flat fan nozzles over 20 images a) distilled water F1 nozzle, b) surfactant solution F1 nozzle, c) distilled water F2 nozzle, d) surfactant solution F2 nozzle, e) distilled water F3 nozzle, f) surfactant solution F3 nozzle, g) distilled water F4 nozzle, h) surfactant solution F4 nozzle

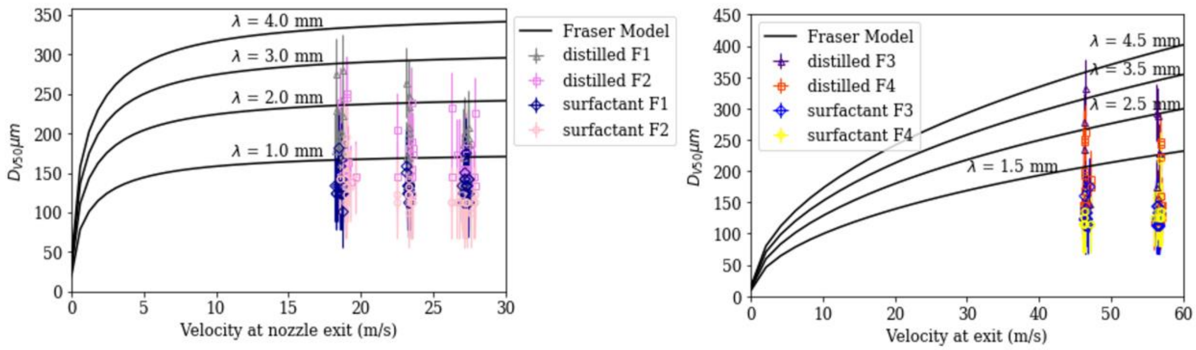

Figure 5.7 Droplet modeling using eq. 19 compared to the measured droplet sizes

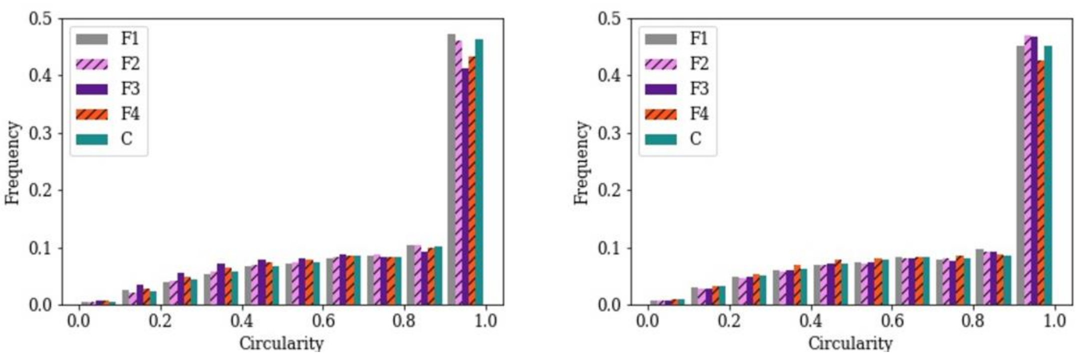

Figure 5.8 Histograms of the circularity of droplets in the fan and cone nozzles at 45 psi. a) distilled water spray, b) surfactant solution spray

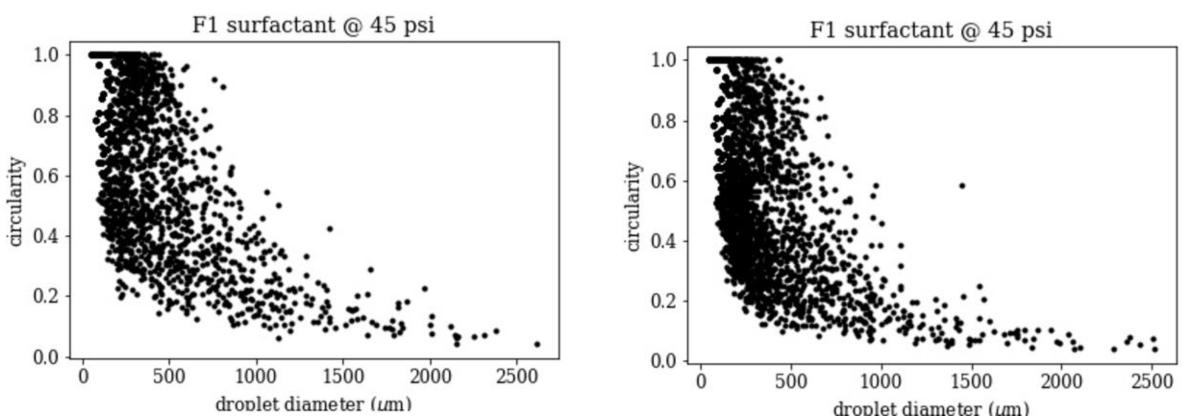

Figure 5.9 The circularity of droplets in F1 compared to the droplet diameter

5.2 Surfactant's effects in bubbler nozzles

In contrast to the fan and cone nozzles, the breakup length increased in the bubbler nozzle (Figure 5.10) with an increase in the spray pressure, in both the distilled spray and the surfactant solution spray (Table 5.3), indicating a different breakup regime. Small disturbances are observed in many of the jet ligaments of the bubbler nozzle before droplets are pinched off the end and formed; jet ligaments experiencing aerodynamic effects before droplets are formed are also observed (Figure 5.11).

The bubbler nozzle experiences Rayleigh and first wind breakup. In Rayleigh breakup regime, the breakup length increases linearly with the increasing velocity of the jet spray (Figure 5.12) [82, 114, 129]. A breakup length model for Rayleigh breakup (eq. 6) depends on the *We* and *Oh* numbers which both depend inversely proportional on the surface tension of the fluid $\left(We \sim \frac{1}{\sigma}, Oh \sim \frac{1}{\sqrt{\sigma}}\right)$;

$$L_b = 19.5 d_{jet} We^{0.5} (1 + 3Oh)^{0.85} \qquad \textbf{20}$$

therefore, the Rayleigh breakup length model depends inversely on the surface tension. The decrease in surface tension increases the breakup length (Figure 5.12). As the velocity increases, the effects of the surface tension grow; the difference between the breakup lengths for the distilled water versus surfactant solution are expected to be larger [82, 131]. Additionally, it can be seen that with larger jet diameters, the breakup length also increases. In the bubbler nozzle spray, both the decrease in surface tension (Figure 5.13 and Table 5.3) and the increased jet/ligament diameters (Figure 5.14) result in increased breakup length in accordance with the Rayleigh expectation. The droplet diameters are larger than or equal to the jet diameter they break off from (e.g. for 10 psi distilled water $d_{jet} = 2.75\ mm < d_{droplet} = 5.34\ mm$) in line with the expectation of droplets from Rayleigh and first wind jet break up [82, 114, 127, 128].

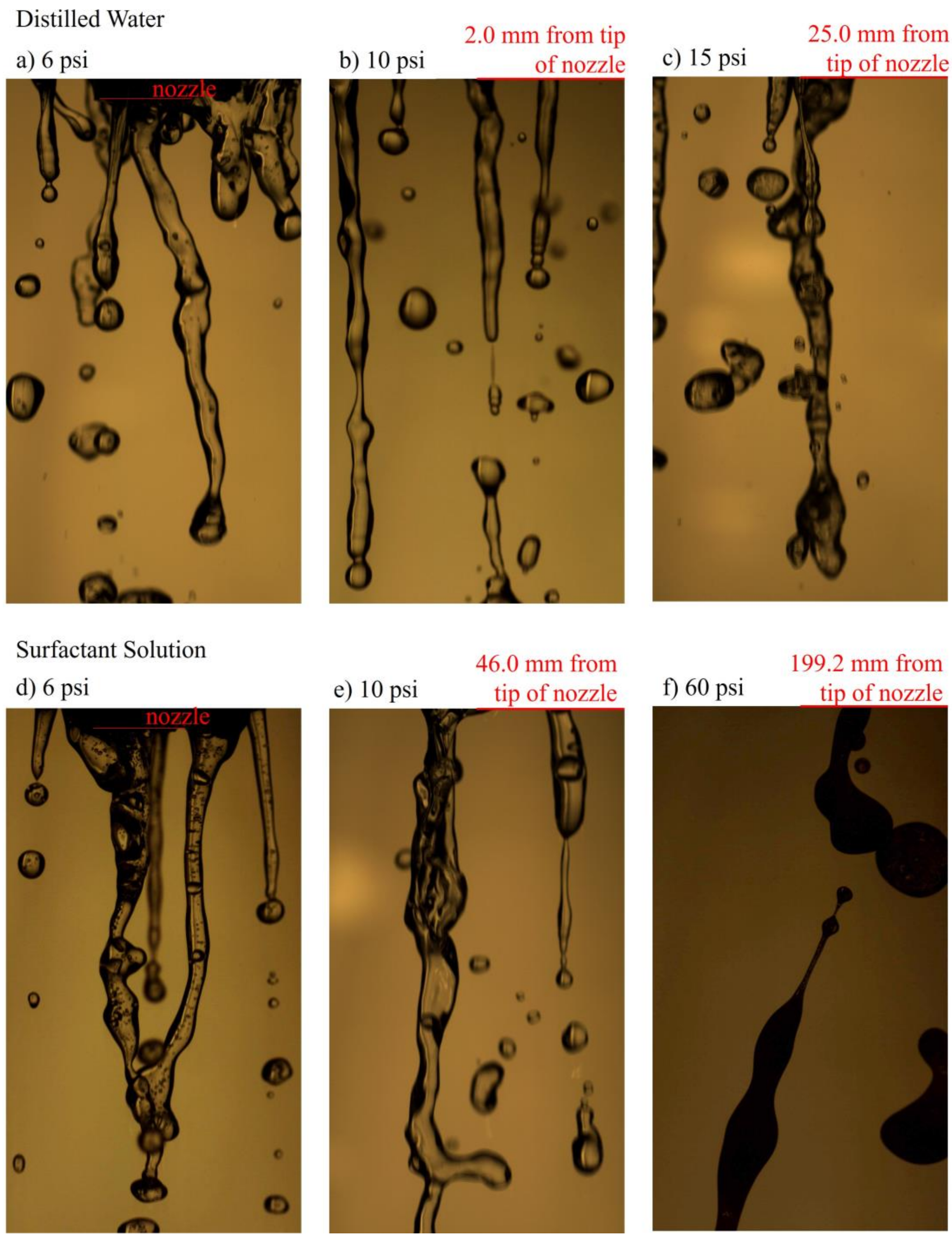

Figure 5.10 Spray from bubbler nozzles a) 6 psi bubbler nozzle distilled water spray with nozzle tip in view, b) 10 psi bubbler nozzle distilled water spray with top of image 2.0 mm from the tip of the nozzle, c) 15 psi bubbler nozzle distilled water spray with top of image 25.0 mm from tip of the nozzle, d) 6 psi bubbler nozzle surfactant solution spray with nozzle tip in view, e) 10 psi bubbler nozzle surfactant solution spray with top of image 46.0 mm from the tip of the nozzle, f) 15 psi bubbler nozzle surfactant solution spray 199.2 mm from the tip of the nozzle

Table 5.3 Breakup length of the bubbler nozzles at various operating pressures under different spray conditions

Nozzle	Pressure	Distilled spray L_b (mm)	Surfactant solution spray L_b (mm)	Distilled d_{jet} (mm)	Surfactant solution d_{jet} (mm)
B1	6 psi (41.4 kPa)	34.6	39.7	2.67	2.52
B2	10 psi (68.9 kPa)	46.8	77.2	2.75	3.41
B3	15 psi (103.4 kPa)	58.8	259.1	2.92	5.72

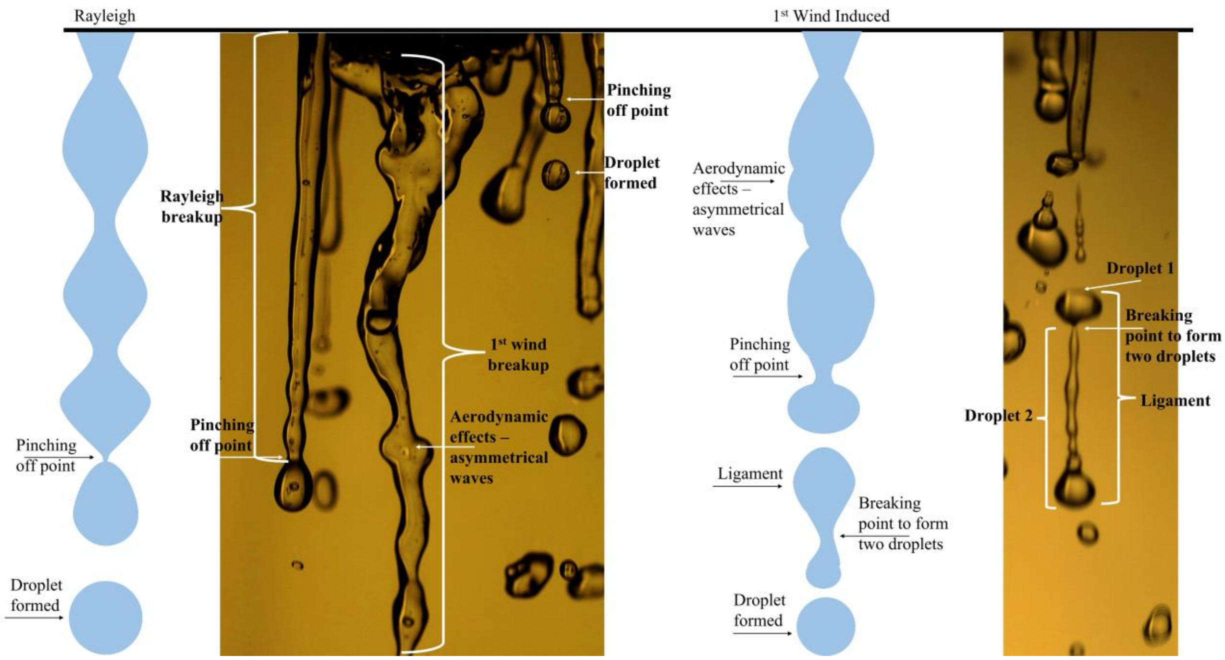

Figure 5.11 Comparison of Figure 3.1 Rayleigh and first wind breakup mechanisms to experimental images. In Rayleigh breakup symmetric waves are observed and a pinching off point for droplet formation from the jet is seen. In first wind breakup asymmetrical waves are observed, ligaments can break off of the main jet before forming into droplets, and a pinching off point from the jet is observed.

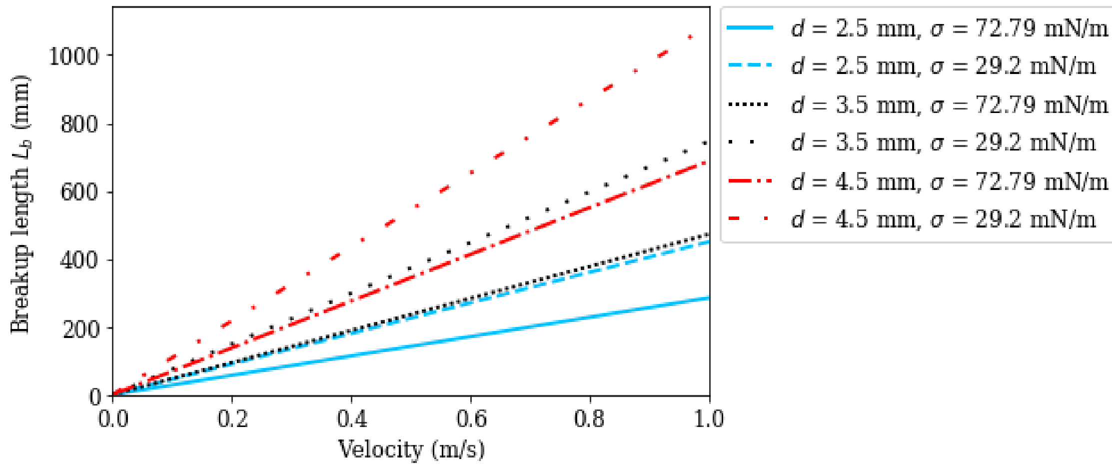

Figure 5.12 Predicted breakup length based on velocity at various jet diameters (2.5, 3.5, and 4.5 mm) for distilled water (σ=72.79 mN/m) and surfactant solution (σ=29.2 mN/m), using eq. 6

5.2.1 Effects of surfactant on breakup length in bubbler nozzles

The addition of surfactant increases the breakup length in the bubbler nozzles; the effects are more prominent at the higher pressures (i.e., higher velocities) (Figure 5.13), as expected compared to the predictive values for increasing velocity in Figure 5.12. The average breakup length for the 6 psi bubbler increases by 5.1 mm (15%), for the 10 psi bubbler nozzle it increases by 30.4 mm (65%), and for the 15 psi bubbler nozzle by 187.7 mm (341%). In addition to the effect on the breakup length, the surfactant impacts the ligament diameter of the bubbler nozzle (Figure 5.13 and Table 5.3). These jets or ligaments formed from the liquid flowing over the bubbler plate and are used as an equivalent to jet diameter for predictive equations. The 6 psi bubbler nozzle experiences a negligible decrease in the average ligament diameter of 0.15 mm. The 10 psi bubbler nozzle experiences a slight increase in the average ligament diameter of 0.66 mm. The 15 psi bubbler nozzle experienced an increase in the average ligament diameter of 1.48 mm. The increased ligament size creates a larger barrier to breakup (i.e., the necessary wave amplitude to prompt breakup is larger), thereby increasing the breakup length, similar to how increasing the nozzle orifice diameter increases the breakup length. The amplitude of disturbances must be larger to result in breakup. The surfactant solution results in ligaments forming together into fewer, larger ligaments, compared to the distilled water.

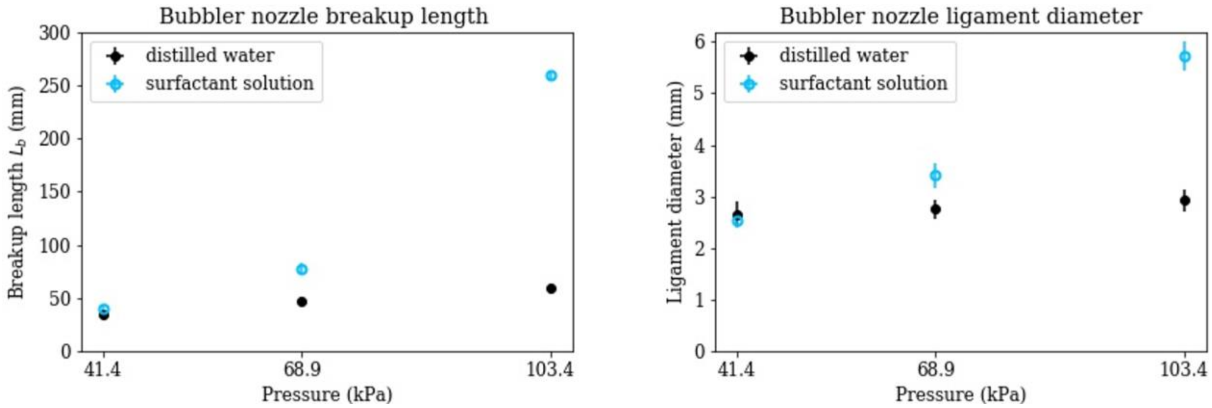

Figure 5.13 Graphs of the bubbler nozzle average breakup length and average ligament diameter for 41.4, 68.9, and 103.4 kPa (6, 10, and 15 psi)

While the ligament of jet diameter plays a role in the increased breakup length, the surfactant's decrease of the surface tension also is important. As can be observed in Figure 5.14, for 10 and 15 psi the breakup length for similarly sized ligaments tends to be larger for the surfactant solution compared to the distilled water; this is more readily visible for the 15 psi bubbler. For the 6 psi bubbler, this is not as readily seen; the breakup length is similar for the distilled water and surfactant solution. This is in-line with eq. 6 which predicts larger breakup lengths for smaller surface tensions and a greater effect with higher velocities.

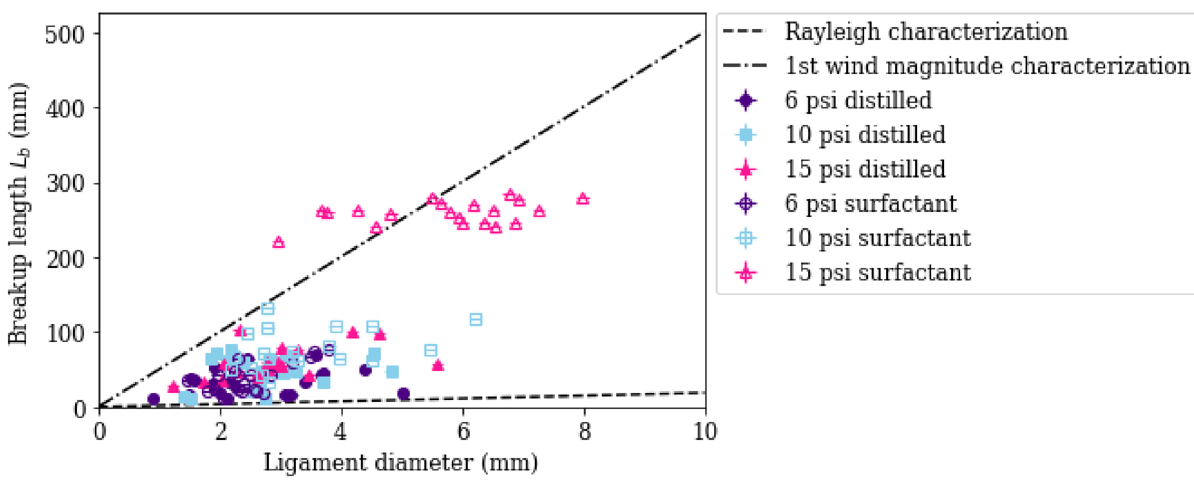

Figure 5.14 The breakup length compared to the ligament diameter for the bubbler nozzle with the Rayleigh predicted breakup length and the 1st wind predicted breakup length magnitude

5.2.2 Surfactant's effects on droplet size in bubbler nozzle

The initial droplet diameters are either around the same size as the ligament diameter or are larger, again, indicating Rayleigh breakup and first wind breakup (Figure 5.15). The droplet diameters for the distilled water have a standard deviation of 1.2 mm, 0.9 mm, and 1.6 mm for 6, 10, and 15 psi, respectively; for the surfactant solution spray, the droplet diameters have a standard deviation of 1.6 mm, 1.5 mm, and 2.3 mm for 6, 10, and 15 psi, respectively. The increase in deviation for the 15 psi bubbler nozzle is due to the increase in breakup length. In contrast to the fan and cone nozzles, the addition of surfactant to distilled water in the bubbler nozzle increases the droplet size for the B2 and B3 and decreases the droplet size minimally in B1 (Figure 5.16 and Table 5.4). The B1 nozzle droplet diameter decrease of 0.40 mm (8%) is in line with the small decrease in ligament size. Additionally, with the increase of the ligament diameter of B2 and B3, the initial droplet diameter also increases; 0.75 mm (14%) and 4.18 mm (69%) respectively. Since the ligament diameter and the breakup length are directly related, there is also a correlation between the breakup length and the droplet size; as the breakup length increase, the droplet size increases (Figure 5.17).

Due to the design of bubbler nozzles, Rayleigh breakup is experienced, and the breakup length and droplet diameter is dependent on the initial jets or ligaments formed coming off the bubbler plate. The breakup length is then further impacted by the surface tension of the fluid; Rayleigh breakup occurs due to the effects of surface tension forces.

Larger velocities can be seen in from the bubbler nozzle droplets due to the increased droplet sizes having a larger terminal velocity (Figure 5.18). Increasing the velocity, size of the droplets, and breakup length results in less time for droplets to risk experiencing drift. These velocities could also impact soil infiltration. However, differing droplet sizes impact coverage, soil infiltration, and soil water distribution.

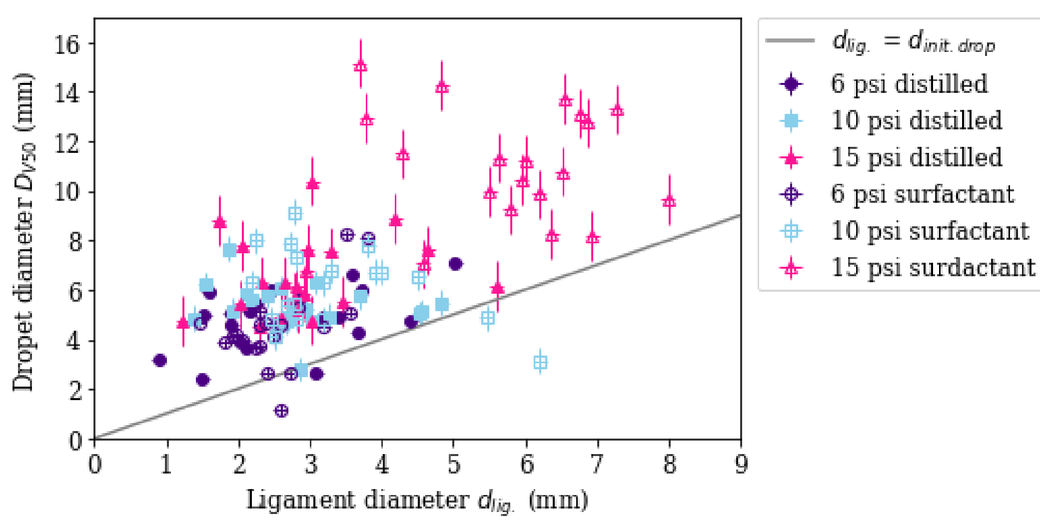

Figure 5.15 The droplet diameter compared to the bubbler ligament's diameter. Droplet sizes similar to or greater than the ligament's diameter are a characteristic of Rayleigh breakup ($d_{lig.} = d_{init.drop}$)

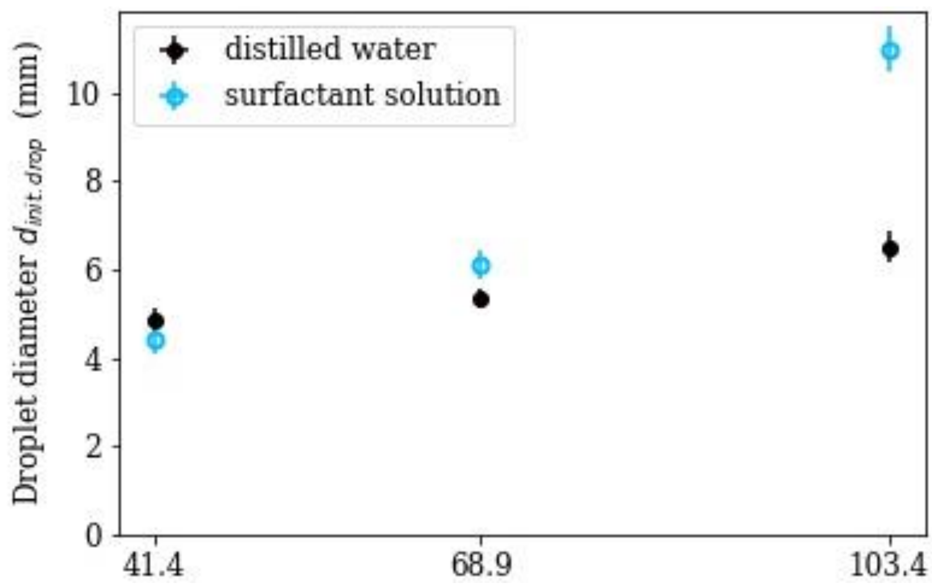

Figure 5.16 Graph of average initial droplet diameter formed from bubbler nozzle ligament

Table 5.4 Average initial droplet diameter for the bubbler nozzle at various spray conditions

Nozzle	Pressure	Distilled Spray Droplet Diameter (µm)	Surfactant Solution Spray Droplet Diameter (µm)
B1	6 psi (41.4 kPa)	4849.1	4444.3
B2	10 psi (68.9 kPa)	5336.1	6086.7
B3	15 psi (103.4 kPa)	6510.6	10973.3

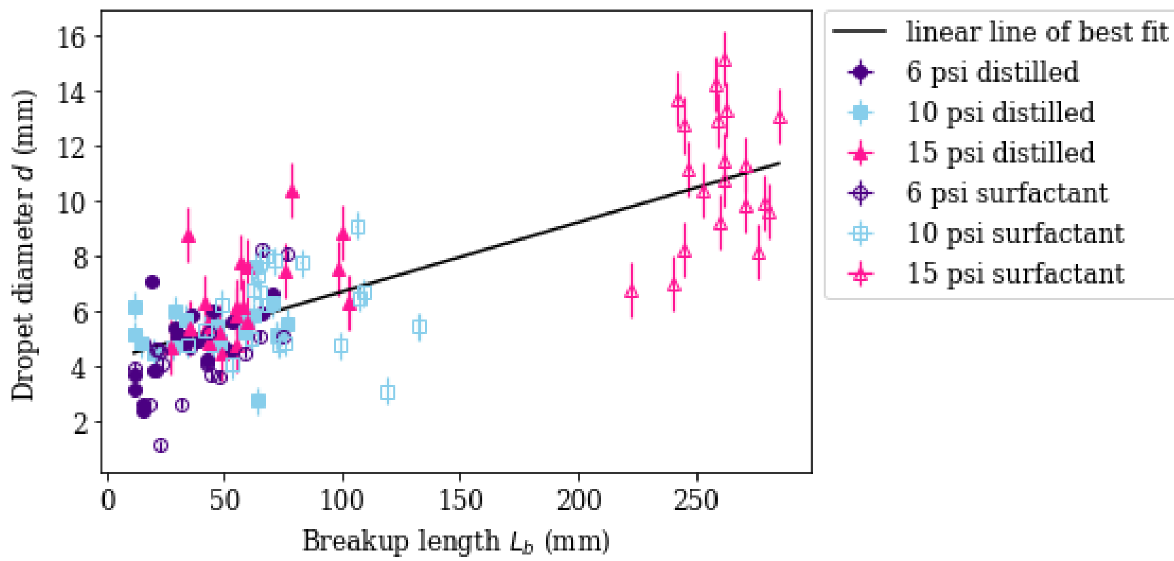

Figure 5.17 The droplet diameter compared to the breakup length for the bubbler nozzle with a best fit line $d = 0.0268L_b + 4.057$

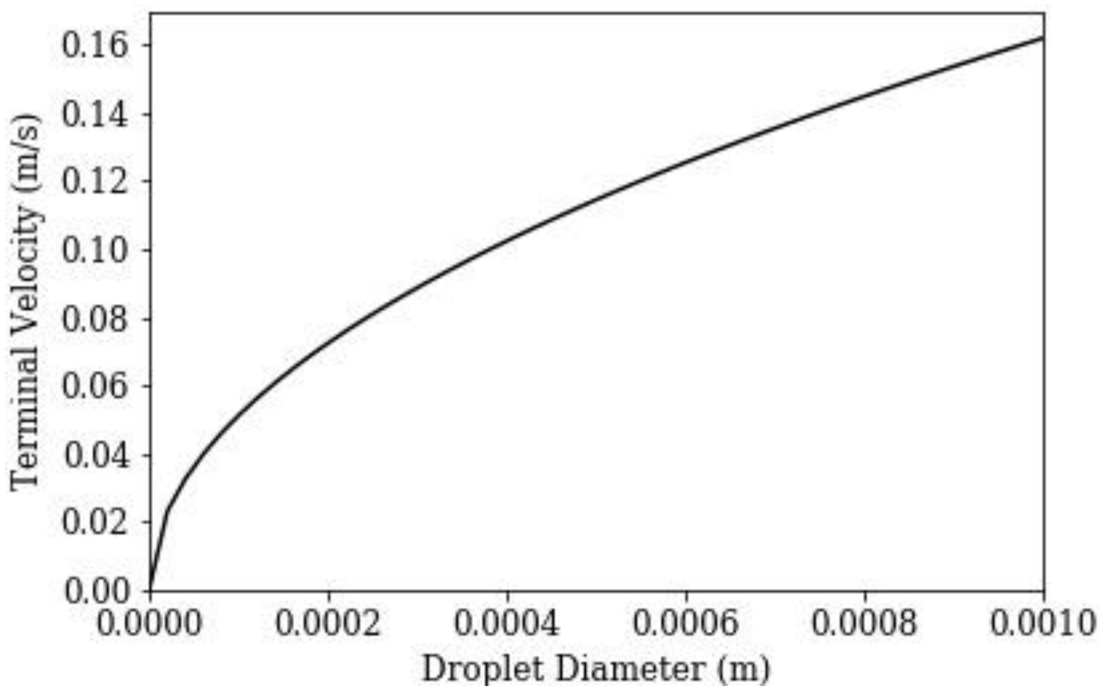

Figure 5.18 Terminal velocity for droplet diameters up to 1 mm

Chapter 6 - Conclusions and Future Work

The droplet dynamics for freezing in grooved and sintered heat pipe wicks and the spray dynamics from fan, cone, and bubbler nozzles were investigated. Understanding the freezing mechanisms on wicking surfaces can lead to wick designs that can mitigate the damaging effects of heat pipe freezing. The topography of the surfaces has greater impacts on the freezing time by influencing the freezing mechanisms and the speed at which the freezing front can propagate. Conclusions for the freezing droplet dynamics are[3]:

- The plain copper surface can employ ice bridging across its entire length, with minimal interference. Therefore, a majority of the droplets formed on the surface resulted in a bridging parameter of less than one.
- The grooved surfaces employ ice bridging as well ($S^* < 1$), the droplet-to-droplet interaction is restricted to droplets along the same groove. Droplet bridging from the top of one groove to another fails due to the S^*>1, thereby increasing the time for the grooved surface to freeze, as each groove must freeze individually.
- The sintered surfaces employ a mixture of ice bridging ($S^* < 1$), stochastic freezing, and cascade freezing.
- The freezing times on the sintered wick were the most varied of the three surfaces, had the most varied freezing start times, as well as the longest freezing start and end times, as a result of the differing area taken up by voids. The varied freezing times result from the dry zone voids ($S^* > 1$) created by the sintered particles and the sintered particles themselves acting as surface defects or edges.
- The void structure and surface energy could be tailored to simultaneously allow for wicking the liquid state but prevent ice bridging and cascade freezing mechanism.

Understanding the effects of surfactant on droplet dynamics is integral in investigating methods to reduce irrigation water without altering crop yields. The spraying of a surfactant solution can be used to introduce Surfactin to the soil. Conclusions for the spray droplet dynamics are:

[3] E. M. Stallbaumer-Cyr, M. M. Derby, and A. R. Betz, "Physical mechanisms for delaying condensation freezing on grooved and sintered wicking surfaces," Applied Physics Letters, vol. 121, p. 071601, 2022., with permission from AIP publishing

- The surfactant solution results in an increased breakup length in the fan, cone, and bubbler nozzles, contrary to decreasing the surface tension with pure liquids. The breakup length for the fan nozzles increased between 5% and 48%, the cone nozzle increased between 6% and 28%, and the bubbler nozzle increased between 15% to 341%.
- The addition of surfactant increases the breakup length due to the effects of the dynamic surface tension for the fan, cone, and bubbler nozzles.
- In line with the increase in breakup length, the surfactant solution decreases the volumetric median droplet diameter in the fan nozzle between 4% and 33%.
- The median diameter of the droplets for the fan nozzle were compared to the model developed by Fraser et al. [92]. The distilled water droplets matched with varying wavelengths and the surfactant solution's droplets were overpredicted due to the use of the equilibrium surface tension.
- The surfactant solution decreases the volumetric median droplet diameter in the cone nozzle for 20 psi, 30 psi, and 45 psi (137.9, 206.8, and 310.3 kPa), but increases it for 60 psi (413.7 kPa). This is likely due to the more 3D effects of this nozzle.
- The surfactant solution increased the ligament sizes of the bubbler nozzles thereby increasing the size of the droplets 14% at 10 psi (68.9 kPa) and 69% at 15 psi (103.4 kPa), in line with Rayleigh breakup.

The decrease in droplet size for the fan and cone nozzles may increase the risk of drift as well as affect the distribution of the water and surfactant in the soil; while the increase in the droplet size for the bubbler nozzle will decrease the risk of drift but also could affect the distribution of water and surfactant in soil. Future research includes understanding how the addition of surfactant in a spray solution affects the water distribution within soil and its ability to transport horizontally due to capillary action, as is required of the bubbler nozzles. Additionally, surfactant's effect on droplet dynamics for other designed for larger droplets can be further investigated.

Chapter 7 - Nomenclature

A	Area
A_{IL}	Contact area of ice and water
A_{IW}	Contact area of ice and the wall of the surface
b	Characteristic length
C	Dimensionless constant
d	Diameter
D_h	Hydraulic diameter
D_{V50}	Volumetric median diameter
ΔG	Change in Gibbs free energy
$\Delta\widetilde{g_V}$	Change in energy per volume between water and ice
h	Half sheet thickness
k	Wave number
K_s	Wave number corresponding to maximum growth rate
L_b	Breakup length
μ	Viscosity
Oh	Ohnesorge number
Re	Reynolds number
ρ	Density
S^*	Bridging parameter
σ	Surface tension
U	Velocity
V	Volume
We	Weber number
Greek Symbols	
α	$\frac{\rho_{air}}{\rho_l}$
$\ln\left(\frac{\eta_b}{\eta_0}\right)$	Initial disturbance
ω	Growth rate

Ω	Maximum growth rate
Subscripts	
air	Air
droplet	Droplet
hyd	Hydraulic
jet	Jet
l	Liquid
lig	Ligament

References

[1] E. M. Stallbaumer-Cyr, M. M. Derby, and A. R. Betz, "Physical mechanisms for delaying condensation freezing on grooved and sintered wicking surfaces," *Applied Physics Letters,* vol. 121, p. 071601, 2022.

[2] M. R. Haque and A. R. Betz, "Frost formation on aluminum and hydrophobic surfaces," in *International Conference on Nanochannels, Microchannels, and Minichannels*, 2018, p. V001T04A001.

[3] M. R. Haque, S. R. Das, and A. R. Betz, "Experimental investigation of condensation and freezing phenomena on hydrophilic and hydrophobic graphene coating," *Applied Thermal Engineering,* vol. 160, p. 113987, 2019.

[4] M. Rejaul Haque, C. Zhu, C. Qu, E. C. Kinzel, and A. Rachel Betz, "Experimental Investigation of Condensation and Freezing Phenomenon on Hydrophilic and Hydrophobic Titanium Nanopillared Glass Surfaces," *Heat Transfer Engineering,* vol. 42, pp. 533-548, 2021.

[5] P. Hao, C. Lv, and X. Zhang, "Freezing of sessile water droplets on surfaces with various roughness and wettability," *Applied physics letters,* vol. 104, p. 161609, 2014.

[6] N. H. Fletcher, "The chemical physics of ice," *The Chemical Physics of Ice,* 2009.

[7] S. Nath, S. F. Ahmadi, and J. B. Boreyko, "How ice bridges the gap," *Soft Matter,* vol. 16, pp. 1156-1161, 2020.

[8] S. Nath, S. F. Ahmadi, and J. B. Boreyko, "A review of condensation frosting," *Nanoscale and Microscale Thermophysical Engineering,* vol. 21, pp. 81-101, 2017.

[9] J. Lehr, J. Keeley, and J. Lehr, "3.8.43 Sprinkler Irrigation," in *Water Encyclopedia, Volumes 1-5,* ed: John Wiley & Sons, pp. 581-582.

[10] ASABE, "Droplet Size Classification," vol. S572.1, ed.

[11] W. C. Hoffmann, B. Fritz, W. Bagley, G. Kruger, R. Henry, and Z. Czaczyk, "Effects of nozzle spray angle on droplet size and velocity," in *Pesticide Formulation and Delivery Systems: 33rd Volume,"Sustainability: Contributions from Formulation Technology"*, ed: ASTM International, 2014.

[12] R. A. Huber, M. Campbell, N. Doughramaji, and M. M. Derby, "Vibration-enhanced droplet motion modes: Simulations of rocking, ratcheting, ratcheting with breakup, and ejection," *Journal of Fluids Engineering,* vol. 141, 2019.

[13] R. A. Huber and M. M. Derby, "Measured dropwise condensation heat transfer coefficients from moist air under near-quiescent conditions," *Science and Technology for the Built Environment,* pp. 1-7, 2022.

[14] J. Rose, Y. Utaka, and I. Tanasawa, "Dropwise Condensation," in *Handbook of Phase Change: Boiling and Condensation,* S. G. Kandlikar, M. Shoji, and V. K. Dhir, Eds., ed: Routledge, 2019.

[15] R. Mittal, R. Ni, and J.-H. Seo, "The flow physics of COVID-19," *Journal of fluid Mechanics,* vol. 894, p. F2, 2020.

[16] A. Konda, A. Prakash, G. A. Moss, M. Schmoldt, G. D. Grant, and S. Guha, "Aerosol filtration efficiency of common fabrics used in respiratory cloth masks," *ACS nano,* vol. 14, pp. 6339-6347, 2020.

[17] M. Manton, "The physics of clouds in the atmosphere," *Reports on Progress in Physics,* vol. 46, p. 1393, 1983.

[18] UNICEF, "Water Security for All," 2021.

[19] A. A. Yancheshme, G. Momen, and R. J. Aminabadi, "Mechanisms of ice formation and propagation on superhydrophobic surfaces: A review," *Advances in Colloid and Interface Science,* vol. 279, p. 102155, 2020.

[20] EPA, "Environmental Impact and Benefit Assessmenet for the Effluent Limitation Guidelines and Standards for the Airport Deicing Catagory," U.S. Environmental Protection Agency2012.

[21] R. Cai, P. Bai, H. Wang, Y. Luo, X. Chen, G. Wu*, et al.*, "Experimental investigation of the heat transfer performance of a novel double independent chambers casing heat pipe applied for heat dissipation at low temperatures," *Applied Thermal Engineering*, vol. 188, p. 116508, 2021.

[22] K. Shukla, "Heat pipe for aerospace applications—an overview," *Journal of Electronics Cooling and Thermal Control,* vol. 5, p. 1, 2015.

[23] G. Y. Eastman, "The heat pipe," *Scientific American,* vol. 218, pp. 38-47, 1968.

[24] A. Faghri, "Heat pipes: review, opportunities and challenges," *Frontiers in Heat Pipes (FHP),* vol. 5, 2014.

[25] W. Chen, "A Multi-Environment Thermal Control System With Freeze-Tolerant Radiator," in *43rd International Conference on Environmental Systems*, 2013, p. 3354.

[26] M. Ababneh, C. Tarau, W. Anderson, A. Alvarez-Hernandez, S. Ortega, J. Farmer*, et al.*, "Demonstration of Copper-Water Heat Pipes Embedded in High Conductivity (HiK™) Plates in the Advanced Passive Thermal eXperiment (APTx) on the International Space Station," 2018.

[27] K.-L. Lee, C. Tarau, and W. G. Anderson, "Titanium water heat pipe radiators for space fission system thermal management," in *Proceedings of the Joint 19th International Heat Pipe Conference and 13th International Heat Pipe Symposium*, 2018.

[28] J. Ku, L. Ottenstein, and A. Krimchansky, "Investigation of Freeze/Thaw Cycles of a Gas-Charged Heat Pipe," in *43rd AIAA Thermophysics Conference*, 2012, p. 2749.

[29] J. Cepeda-Rizo, "The Problem of Freezing of Copper Water Heat Pipes," presented at the Thirty-Fourth Annual Workshop on Mathematical Problems in Industry, 2018.

[30] A. Faghri, "Frozen start-up behavior of low-temperature heat pipes," *International journal of heat and mass transfer,* vol. 35, pp. 1681-1694, 1992.

[31] J. Ochterbeck and G. Peterson, "Freeze/thaw characteristics of a copper/water heat pipe-Effects ofnoncondensible gas charge," *Journal of thermophysics and heat transfer,* vol. 7, pp. 127-132, 1993.

[32] S. Nath and J. B. Boreyko, "On localized vapor pressure gradients governing condensation and frost phenomena," *Langmuir,* vol. 32, pp. 8350-8365, 2016.

[33] K.-S. Lee, S. Jhee, and D.-K. Yang, "Prediction of the frost formation on a cold flat surface," *International journal of heat and mass transfer,* vol. 46, pp. 3789-3796, 2003.

[34] C. J. Hermes, R. O. Piucco, J. R. Barbosa Jr, and C. Melo, "A study of frost growth and densification on flat surfaces," *Experimental Thermal and Fluid Science,* vol. 33, pp. 371-379, 2009.

[35] Y. Zhang, M. R. Klittich, M. Gao, and A. Dhinojwala, "Delaying frost formation by controlling surface chemistry of carbon nanotube-coated steel surfaces," *ACS applied materials & interfaces,* vol. 9, pp. 6512-6519, 2017.

[36] Z.-J. Wang, D.-J. Kwon, K. L. DeVries, and J.-M. Park, "Frost formation and anti-icing performance of a hydrophobic coating on aluminum," *Experimental Thermal and Fluid Science,* vol. 60, pp. 132-137, 2015.

[37] M. R. Haque, *Understanding and controlling condensation and frosting phenomena on engineered surfaces*: Kansas State University, 2019.
[38] M. A. Muntaha, M. M. Haider, and M. A. Rahman, "Modelling of frost formation and growth on microstuctured surface," in *AIP Conference Proceedings*, 2016, p. 050042.
[39] Y. Shen, H. Zou, and S. Wang, "Condensation frosting on micropillar surfaces–effect of microscale roughness on ice propagation," *Langmuir,* vol. 36, pp. 13563-13574, 2020.
[40] W. Sheng, Y. Pei, X. Li, P. Ming, and W. Zhao, "Effect of surface characteristics on condensate droplets growth," *Applied Thermal Engineering,* vol. 173, p. 115260, 2020.
[41] P. Eberle, M. K. Tiwari, T. Maitra, and D. Poulikakos, "Rational nanostructuring of surfaces for extraordinary icephobicity," *Nanoscale,* vol. 6, pp. 4874-4881, 2014.
[42] R. Bohm, M. R. Haque, C. Qu, E. C. Kinzel, and A. R. Betz, "Accelerated freezing due to droplet pinning on a nanopillared surface," *AIP Advances,* vol. 8, p. 125228, 2018.
[43] Y. Zhao, R. Wang, and C. Yang, "Interdroplet freezing wave propagation of condensation frosting on micropillar patterned superhydrophobic surfaces of varying pitches," *International Journal of Heat and Mass Transfer,* vol. 108, pp. 1048-1056, 2017.
[44] Y. Zhao and C. Yang, "Frost spreading on microscale wettability/morphology patterned surfaces," *Applied Thermal Engineering,* vol. 121, pp. 136-145, 2017.
[45] F. M. Ruiz-Cabello, S. Bermúdez-Romero, P. F. Ibanez-Ibanez, M. Cabrerizo-Vilchez, and M. Rodríguez-Valverde, "Freezing delay of sessile drops: Probing the impact of contact angle, surface roughness and thermal conductivity," *Applied Surface Science,* vol. 537, p. 147964, 2021.
[46] M. M. Mekonnen and A. Y. Hoekstra, "Four billion people facing severe water scarcity," *Science advances,* vol. 2, p. e1500323, 2016.
[47] FAO, "Overcoming water challenges in agriculture.," ed, 2020.
[48] U. Nations. (2019). *Growing at a slower pace, world population is expected to reach 9.7 billion in 2050 and could peak at nearly 11 billion around 2100*. Available: https://www.un.org/development/desa/en/news/population/world-population-prospects-2019.html
[49] S. Siebert, J. Burke, J.-M. Faures, K. Frenken, J. Hoogeveen, P. Döll, *et al.*, "Groundwater use for irrigation–a global inventory," *Hydrology and earth system sciences,* vol. 14, pp. 1863-1880, 2010.
[50] M. M. Gutierrez, M. V. Cameron-Harp, P. P. Chakraborty, E. M. Stallbaumer-Cyr, J. A. Morrow, R. R. Hansen, *et al.*, "Investigating a microbial approach to water conservation: Effects of Bacillus subtilis and Surfactin on evaporation dynamics in loam and sandy loam soils," *Frontiers in Sustainable Food Systems,* p. 441, 2022.
[51] D. o. W. Services. Water Use Data Collection and Use [Fact Sheet] [Online]. Available: https://agriculture.ks.gov/docs/default-source/dwr-water-appropriation-documents/waterusedatacollection-2015b0d5d4002e6262e1aa5bff0000620720.pdf?sfvrsn=61b7b6c1_14
[52] USDA. *Irrigation & Water Use*. Available: https://www.ers.usda.gov/topics/farm-practices-management/irrigation-water-use/
[53] USGS. (2019). *Irrigation Water Use*. Available: https://www.usgs.gov/mission-areas/water-resources/science/irrigation-water-use?qt-science_center_objects=0#qt-science_center_objects
[54] USDA, "Land Values 2022 Summary August 2022," United States Department of Agriculture2022.

[55] B. Na and R. L. Webb, "A fundamental understanding of factors affecting frost nucleation," *International Journal of Heat and Mass Transfer,* vol. 46, pp. 3797-3808, 2003.
[56] A. S. Van Dyke, D. Collard, M. M. Derby, and A. R. Betz, "Droplet coalescence and freezing on hydrophilic, hydrophobic, and biphilic surfaces," *Applied Physics Letters,* vol. 107, p. 141602, 2015.
[57] M.-H. Kim, H. Kim, K.-S. Lee, and D. R. Kim, "Frosting characteristics on hydrophobic and superhydrophobic surfaces: A review," *Energy Conversion and Management,* vol. 138, pp. 1-11, 2017.
[58] J. McCormick and J. Westwater, "Nucleation sites for dropwise condensation," *Chemical Engineering Science,* vol. 20, pp. 1021-1036, 1965.
[59] J. B. Boreyko, R. R. Hansen, K. R. Murphy, S. Nath, S. T. Retterer, and C. P. Collier, "Controlling condensation and frost growth with chemical micropatterns," *Scientific reports,* vol. 6, pp. 1-15, 2016.
[60] G. Graeber, V. Dolder, T. M. Schutzius, and D. Poulikakos, "Cascade freezing of supercooled water droplet collectives," *ACS nano,* vol. 12, pp. 11274-11281, 2018.
[61] E. Stallbaumer, A. Cernas, A. Betz, and M. Derby, "Ice Formation due to Condensation of Moist Air on Commercial Wicks," in *International Conference on Nanochannels, Microchannels, and Minichannels,* 2020, p. V001T03A004.
[62] I. Makhnenko, E. R. Alonzi, S. A. Fredericks, C. M. Colby, and C. S. Dutcher, "A review of liquid sheet breakup: Perspectives from agricultural sprays," *Journal of Aerosol Science,* vol. 157, p. 105805, 2021.
[63] S. Kooij, R. Sijs, M. M. Denn, E. Villermaux, and D. Bonn, "What determines the drop size in sprays?," *Physical Review X,* vol. 8, p. 031019, 2018.
[64] R. Chen, H. Li, J. Wang, X. Guo, and Z. Song, "Comparisons of Spray Characteristics between Non-circular and Circular Nozzles with Rotating Sprinklers," *Applied Engineering in Agriculture,* vol. 38, pp. 61-75, 2022.
[65] J. Wang, Z. Song, R. Chen, T. Yang, and Z. Tian, "Experimental Study on Droplet Characteristics of Rotating Sprinklers with Circular Nozzles and Diffuser," *Agriculture,* vol. 12, p. 987, 2022.
[66] Y. Li, G. Bai, and H. Yan, "Development and validation of a modified model to simulate the sprinkler water distribution," *Computers and Electronics in Agriculture,* vol. 111, pp. 38-47, 2015.
[67] Y. Jiang, H. Li, C. Chen, L. Hua, and D. Zhang, "Hydraulic performance and jet breakup characteristics of the impact sprinkler with circular and non-circular nozzles," *Applied engineering in agriculture,* vol. 35, pp. 911-924, 2019.
[68] O. Adeyemi, I. Grove, S. Peets, and T. Norton, "Advanced monitoring and management systems for improving sustainability in precision irrigation," *Sustainability,* vol. 9, p. 353, 2017.
[69] J. Fontela. (2018, April 2018) Lower pressure for higher efficiency. *Irrigation Today*. 25-26. Available: http://www.modernpubsonline.com/0A406ys/IrrigationTodayApr18/html/index.html?page=24&origin=reader
[70] R. T. Peters, H. Neibling, R. Stroh, B. Molaei, and H. Mehanna, "Low energy precision application (LEPA) and low elevation spray application (LESA) trials in the Pacific Northwest," in *Proceedings of 2016 California Alfalfa and Forage Symposium,* 2016, pp. 1-21.

[71] T. J. Trout and D. C. Kincaid, "On-Farm System Design and Operation and Land Management," in *Irrigaton of Agricultural Crops*, R. J. Lascano and R. E. Sojika, Eds., Second Edition ed Madison, WI: American Society of Agronomy Inc., 2007.
[72] T. E. Oker, A. Y. Sheshukov, J. Aguilar, D. H. Rogers, and I. Kisekka, "Evaluating Soil Water Redistribution under Mobile Drip Irrigation, Low-Elevation Spray Application, and Low-Energy Precision Application Using HYDRUS," *Journal of Irrigation and Drainage Engineering,* vol. 147, p. 04021016, 2021.
[73] M. Butler Ellis and C. Tuck, "How adjuvants influence spray formation with different hydraulic nozzles," *Crop protection,* vol. 18, pp. 101-109, 1999.
[74] S. Wang, G. Dorr, M. Khashehchi, and X. He, "Performance of selected agricultural spray nozzles using particle image velocimetry," *Journal of Agricultural Science and Technology,* vol. 17, pp. 601-613, 2015.
[75] A. Asgarian, M. Heinrich, R. Schwarze, M. Bussmann, and K. Chattopadhyay, "Experiments and modeling of the breakup mechanisms of an attenuating liquid sheet," *International Journal of Multiphase Flow,* vol. 130, p. 103347, 2020.
[76] R. Sijs and D. Bonn, "The effect of adjuvants on spray droplet size from hydraulic nozzles," *Pest Management Science,* vol. 76, pp. 3487-3494, 2020.
[77] M. Nadeem, T. Nguyen-Quang, C. Diallo, U. Venkatadri, and P. Havard, "Contribution to spraying nozzle study: a comparative investigation of imaging and simulation approaches," *Pakistan Journal of Agricultural Sciences,* vol. 56, 2019.
[78] A. Davanlou, J. D. Lee, S. Basu, and R. Kumar, "Effect of viscosity and surface tension on breakup and coalescence of bicomponent sprays," *Chemical engineering science,* vol. 131, pp. 243-255, 2015.
[79] A. Sinha, S. Balasubramanian, and S. Gopalakrishnan, "A numerical study on dynamics of spray jets," *Sadhana,* vol. 40, pp. 787-802, 2015.
[80] A. Saha, J. D. Lee, S. Basu, and R. Kumar, "Breakup and coalescence characteristics of a hollow cone swirling spray," *Physics of fluids,* vol. 24, p. 124103, 2012.
[81] J. Lee, A. Saha, S. Basu, and R. Kumar, "Effects of injection pressure on spray atomization characteristics with measurement technique cross-validation," in *Proceedings of the 12th Triennial International Conference on Liquid Atomization and Spray Systems, Heidelberg, Germany*, 2012, pp. 2-6.
[82] F. Wang and T. Fang, "Liquid jet breakup for non-circular orifices under low pressures," *International Journal of Multiphase Flow,* vol. 72, pp. 248-262, 2015.
[83] R. Sijs, S. Kooij, and D. Bonn, "How surfactants influence the drop size in sprays from flat fan and hollow cone nozzles," *Physics of Fluids,* vol. 33, p. 113608, 2021.
[84] M. Butler Ellis, C. Tuck, and P. Miller, "The effect of some adjuvants on sprays produced by agricultural flat fan nozzles," *Crop protection,* vol. 16, pp. 41-50, 1997.
[85] K. Qin, H. Tank, S. Wilson, B. Downer, and L. Liu, "Controlling droplet-size distribution using oil emulsions in agricultural sprays," *Atomization and Sprays,* vol. 20, 2010.
[86] M. Butler Ellis, C. Tuck, and P. Miller, "How surface tension of surfactant solutions influences the characteristics of sprays produced by hydraulic nozzles used for pesticide application," *Colloids and Surfaces A: Physicochemical and Engineering Aspects,* vol. 180, pp. 267-276, 2001.
[87] Z. Liu, Z. Li, J. Liu, J. Wu, Y. Yu, and J. Ding, "Numerical Study on Primary Breakup of Disturbed Liquid Jet Sprays Using a VOF Model and LES Method," *Processes,* vol. 10, p. 1148, 2022.

[88] H. Squire, "Investigation of the instability of a moving liquid film," *British Journal of Applied Physics,* vol. 4, p. 167, 1953.
[89] P. Senecal, D. P. Schmidt, I. Nouar, C. J. Rutland, R. D. Reitz, and M. Corradini, "Modeling high-speed viscous liquid sheet atomization," *International Journal of Multiphase Flow,* vol. 25, pp. 1073-1097, 1999.
[90] J. Waters, D. B. Carrington, and M. M. Francois, "Modeling multiphase flow: Spray breakup using volume of fluids in a dynamics LES FEM method," *Numerical Heat Transfer, Part B: Fundamentals,* vol. 72, pp. 285-299, 2017.
[91] M. Turner, S. Sazhin, J. Healey, C. Crua, and S. Martynov, "A breakup model for transient Diesel fuel sprays," *Fuel,* vol. 97, pp. 288-305, 2012.
[92] R. Fraser, P. Eisenklam, N. Dombrowski, and D. Hasson, "Drop formation from rapidly moving liquid sheets," *AIChE Journal,* vol. 8, pp. 672-680, 1962.
[93] R. W. Dexter, "The effect of fluid properties on the spray quality from a flat fan nozzle," *ASTM SPECIAL TECHNICAL PUBLICATION,* vol. 1400, pp. 27-43, 2001.
[94] M. Broumand, A. Asgarian, M. Bussmann, K. Chattopadhyay, and M. Thomson, "Spatio-temporal dynamics and disintegration of a fan liquid sheet," *Physics of Fluids,* vol. 33, p. 112109, 2021.
[95] U. Shavit and N. Chigier, "The role of dynamic surface tension in air assist atomization," *Physics of Fluids,* vol. 7, pp. 24-33, 1995.
[96] C. Sula, H. Grosshans, and M. Papalexandris, "Assessment of droplet breakup models for spray flow simulations," *Flow, Turbulence and Combustion,* vol. 105, pp. 889-914, 2020.
[97] E.-S. R. Negeed, S. Hidaka, M. Kohno, and Y. Takata, "Experimental and analytical investigation of liquid sheet breakup characteristics," *International Journal of Heat and Fluid Flow,* vol. 32, pp. 95-106, 2011.
[98] M. Etzold, A. Deswal, L. Chen, and F. Durst, "Break-up length of liquid jets produced by short nozzles," *International Journal of Multiphase Flow,* vol. 99, pp. 397-407, 2018.
[99] K. H. Solomon, D. C. Kincaid, and J. C. Bezdek, "Drop size distributions for irrigation spray nozzles," *Transactions of the ASAE,* vol. 28, pp. 1966-1974, 1985.
[100] S. Li, C. Chen, Y. Wang, F. Kang, and W. Li, "Study on the atomization characteristics of flat fan nozzles for pesticide application at low pressures," *Agriculture,* vol. 11, p. 309, 2021.
[101] N. Dombrowski and R. P. Fraser, "A photographic investigation into the disintegration of liquid sheets," *Philosophical Transactions of the Royal Society of London. Series A, Mathematical and Physical Sciences,* vol. 247, pp. 101-130, 1954.
[102] H. Lienemann, J. Shrimpton, and E. Fernandes, "A study on the aerodynamic instability of attenuating liquid sheets," *Experiments in fluids,* vol. 42, pp. 241-258, 2007.
[103] S. Rezayat, M. Farshchi, and E. Berrocal, "High-speed imaging database of water jet disintegration Part II: Temporal analysis of the primary breakup," *International Journal of Multiphase Flow,* vol. 145, p. 103807, 2021.
[104] L. Broniarz-Press, S. Włodarczak, M. Matuszak, M. Ochowiak, R. Idziak, T. Szulc, *et al.*, "The effect of orifice shape and the injection pressure on enhancement of the atomization process for pressure-swirl atomizers," *Crop Protection,* vol. 82, pp. 65-74, 2016.
[105] M. Das, S. Chatterjee, A. Mukhopadhyay, and S. Sen, "Experimental Investigation of a Hollow Cone Spray Using Laser Diagnostics," *Journal of engineering for gas turbines and power,* vol. 136, 2014.

[106] D. Lohse and E. Villermaux, "Double threshold behavior for breakup of liquid sheets," *Proceedings of the National Academy of Sciences,* vol. 117, pp. 18912-18914, 2020.
[107] J. E. Madero and R. L. Axelbaum, "Spray breakup and structure of spray flames for low-volatility wet fuels," *Combustion and Flame,* vol. 180, pp. 102-109, 2017.
[108] N. Dombrowski and W. Johns, "The aerodynamic instability and disintegration of viscous liquid sheets," *Chemical Engineering Science,* vol. 18, pp. 203-214, 1963.
[109] G. Agbaglah, "Breakup of thin liquid sheets through hole–hole and hole–rim merging," *Journal of Fluid Mechanics,* vol. 911, 2021.
[110] S. L. Post and A. J. Hewitt, "Flat-fan spray atomization model," *Transactions of the ASABE,* vol. 61, pp. 1249-1256, 2018.
[111] J. C. Thompson and J. P. Rothstein, "The atomization of viscoelastic fluids in flat-fan and hollow-cone spray nozzles," *Journal of non-newtonian fluid mechanics,* vol. 147, pp. 11-22, 2007.
[112] M. Son, K. Yu, J. Koo, O. C. Kwon, and J. S. Kim, "Effects of momentum ratio and weber number on spray half angles of liquid controlled pintle injector," *Journal of thermal science,* vol. 24, pp. 37-43, 2015.
[113] R. Ford and C. Furmidge, "The formation of drops from viscous Newtonian liquids sprayed through fan-jet nozzles," *British Journal of Applied Physics,* vol. 18, p. 335, 1967.
[114] R. Reitz and S. Lin, "Drop and spray formation from a liquid jet," *Annu. Rev. Fluid Mech,* vol. 30, p. 85, 1998.
[115] G. Lehrsch, R. Sojka, J. Reed, R. Henderson, and S. Kostka, "Surfactant and irrigation effects on wettable soils: runoff, erosion, and water retention responses," *Hydrological Processes,* vol. 25, pp. 766-777, 2011.
[116] J. Fernández-Gálvez and M. Mingorance, "Vapour and liquid hydrophobic characteristics induced by presence of surfactants in an agricultural soil," *Geoderma,* vol. 154, pp. 321-327, 2010.
[117] M.-A. Lowe, F. Mathes, M. H. Loke, G. McGrath, D. V. Murphy, and M. Leopold, "Bacillus subtilis and surfactant amendments for the breakdown of soil water repellency in a sandy soil," *Geoderma,* vol. 344, pp. 108-118, 2019.
[118] N. Raddadi, L. Giacomucci, R. Marasco, D. Daffonchio, A. Cherif, and F. Fava, "Bacterial polyextremotolerant bioemulsifiers from arid soils improve water retention capacity and humidity uptake in sandy soil," *Microbial Cell Factories,* vol. 17, pp. 1-12, 2018.
[119] L. W. Dekker, K. Oostindie, S. J. Kostka, and C. J. Ritsema, "Effects of surfactant treatments on the wettability of a water repellent grass-covered dune sand," *Soil Research,* vol. 43, pp. 383-395, 2005.
[120] E. G. Polli, G. S. Alves, J. V. de Oliveira, and G. R. Kruger, "Physical–chemical properties, droplet size, and efficacy of dicamba plus glyphosate tank mixture influenced by adjuvants," *Agronomy,* vol. 11, p. 1321, 2021.
[121] R. Defay, G. Pétré, and E. Matijević, "Dynamic surface tension," *Surface and Colloid Science,* pp. 27-81, 1971.
[122] M. J. Rosen and J. T. Kunjappu, "Characteristics features of surfactant," in *Surfactants and interfacial phenomena*, ed: John Wiley & Sons, 2012.
[123] M. J. Rosen and J. T. Kunjappu, "Reduction of surface and interfactial tension by surfactants," in *Surfactants and interfacial phenomena*, ed: John Wiley & Sons, 2012.

[124] J. K. Ferri and K. J. Stebe, "Which surfactants reduce surface tension faster? A scaling argument for diffusion-controlled adsorption," *Advances in Colloid and Interface Science,* vol. 85, pp. 61-97, 2000.
[125] V. Fainerman, R. Miller, and E. Aksenenko, "Simple model for prediction of surface tension of mixed surfactant solutions," *Advances in colloid and interface science,* vol. 96, pp. 339-359, 2002.
[126] V. Bertola and G. Brenn, "Transport Phenomena Across Interfaces of Complex Fluids: Drops and Sprays," in *Transport Phenomena in Complex Fluids*, ed: Springer, 2020, pp. 293-360.
[127] J. Delteil, S. Vincent, A. Erriguible, and P. Subra-Paternault, "Numerical investigations in Rayleigh breakup of round liquid jets with VOF methods," *Computers & Fluids,* vol. 50, pp. 10-23, 2011.
[128] C. Dumouchel, "On the experimental investigation on primary atomization of liquid streams," *Experiments in fluids,* vol. 45, pp. 371-422, 2008.
[129] A. Kalaaji, B. Lopez, P. Attane, and A. Soucemarianadin, "Breakup length of forced liquid jets," *Physics of Fluids,* vol. 15, pp. 2469-2479, 2003.
[130] J. Gordillo and M. Pérez-Saborid, "Aerodynamic effects in the break-up of liquid jets: on the first wind-induced break-up regime," *Journal of Fluid Mechanics,* vol. 541, pp. 1-20, 2005.
[131] R. P. Grant and S. Middleman, "Newtonian jet stability," *AIChE Journal,* vol. 12, pp. 669-678, 1966.
[132] T. Lucchini, G. D'Errico, and N. Nordin, "CFD modelling of gasoline sprays," in *7th International Conference on Engines for Automobile*, 2005.
[133] G. I. Taylor, "The dynamics of thin sheets of fluid. III. Disintegration of fluid sheets," *Proceedings of the Royal Society of London. Series A. Mathematical and Physical Sciences,* vol. 253, pp. 313-321, 1959.
[134] H. Malot and J. B. Blaisot, "Droplet size distribution and sphericity measurements of low-density sprays through image analysis," *Particle & Particle Systems Characterization: Measurement and Description of Particle Properties and Behavior in Powders and Other Disperse Systems,* vol. 17, pp. 146-158, 2000.
[135] H. Zhu, M. Salyani, and R. D. Fox, "A portable scanning system for evaluation of spray deposit distribution," *Computers and Electronics in Agriculture,* vol. 76, pp. 38-43, 2011.
[136] V. Levich and V. Krylov, "Surface-tension-driven phenomena," *Annual review of fluid mechanics,* vol. 1, pp. 293-316, 1969.
[137] M. Weiss, "Surfactant adsorption and Marangoni flow in liquid jets," University of Oxford, 2004.
[138] T. Battal, C. D. Bain, M. Weiß, and R. C. Darton, "Surfactant adsorption and Marangoni flow in liquid jets: I. Experiments," *Journal of colloid and interface science,* vol. 263, pp. 250-260, 2003.

Appendix A - Python Sintered Void Imaging Code

```
# -*- coding: utf-8 -*-
"""
Created on Tue Jul 19 11:07:26 2022

@author: Emily
"""

from PIL import Image

# Import an image from directory:
names = ['1-11-22', '2-22-22', '2-23-22', '2-23-22(2)', '2-24-22', '1-11-2
2 frozen', '2-22-22 frozen', '2-23-22 frozen', '2-23-22(2) frozen', '2-24-
22 frozen']
v = []
nv = []

for string in names:
    input_image = Image.open(string + '.jpg')
    image1 = Image.open(string + '.jpg')
    image2 = Image.open(string + '.jpg')


    # Extracting pixel map:
    pixel_map = input_image.load()

    # Extracting the width and height
    # of the image:
    width, height = input_image.size
    voids = 0
    cont = 0

    kr = [15, 116]
    kg = [3, 59]
    kb = [0, 31]

    ir = [145, 255]
    ig = [64, 166]
    ib = [12,123]

    for i in range(width):
        for j in range(height):

            # getting the RGB pixel value.
            r, g, b = input_image.getpixel((i, j))
            if ir[0]<=r<=ir[1] and ib[0]<=b<=ib[1] and ig[0]<=g<=ig[1]:
                image1.putpixel((i,j), (255,255,255))
                image2.putpixel((i,j), (255,255,255))
                cont+=1
            elif kr[0]<=r<=kr[1] and kb[0]<=b<=kb[1] and kg[0]<=g<=kg[1]:
                image2.putpixel((i,j), (0,0,0))
                voids+=1
            else:
```

```
                image1.putpixel((i,j), (255,255,255))
                image2.putpixel((i,j), (255,255,255))
                cont+=1
    print('\n', string)
    print("voids:", voids)
    print("not voids:", cont)
    print("total:", height*width, height*width == voids+cont)
    print('% voids:', voids/(height*width)*100)

    v.append(voids)
    nv.append(cont)


    # use input_image.show() to see the image on the
    # output screen.

    s1 = string + 'white.jpg'
    image1.save(s1)
    s2 = string + 'blackwhite.jpg'
    image2.save(s2)

    input_image.close()
    image1.close()
    image2.close()
```